The Search for Young Planets with JWST/NIRCam

by

Camryn Mullin
B.Sc., McGill University, 2022

A Thesis Submitted in Partial Fulfillment of the
Requirements for the Degree of

MASTER OF SCIENCE

in the Department of Physics and Astronomy

The Search for Young Planets with JWST/NIRCam

by

Camryn Mullin
B.Sc., McGill University, 2022

Supervisory Committee

Dr. R. Dong, Supervisor
(Department of Physics and Astronomy)

Dr. D. Johnstone, Departmental Member
(Department of Physics and Astronomy)

Abstract

As part of the James Webb Space Telescope (JWST) Guaranteed Time Observation (GTO) program "Direct Imaging of YSOs" (program ID 1179), I used JWST NIRCam's direct imaging mode with filters F187N, F200W, F405N, and F410M to perform high contrast observations of the circumstellar structures surrounding the protostar HL Tau. The data reveal the known stellar envelope, outflow cavity, and streamers, but do not detect any companion candidates. I detect scattered light from an in-flowing spiral streamer previously detected in HCO^+ by the Atacama Large Millimeter/submillimeter Array, and part of the structure connected to the c-shaped outflow cavity. For detection limits in planet mass, I use BEX evolutionary tracks when $M_{\rm p} < 2M_{\rm J}$ and AMES-COND evolutionary tracks otherwise, assuming a planet age of 1 Myr (youngest available age). Inside the disk region, due to extended envelope emission, the point-source sensitivities are $\sim$5 mJy (37 $M_{\rm J}$) at 40 au in F187N, and $\sim$0.37 mJy (5.2 $M_{\rm J}$) at 140 au in F405N. Outside the disk region, the deepest limits I can reach are $\sim$0.01 mJy (0.75 $M_{\rm J}$) at a projected separation of $\sim$525 au.

Table of Contents

List of Tables

List of Figures

Acknowledgements

I would like to thank:

my family, wonderful partner, and friends for supporting me during the difficult periods.

Ruobing Dong, for mentoring, support, encouragement, and patience.

Sciences and Engineering Research Council of Canada (NSERC),

the Alfred P. Sloan Foundation,

and the New Frontiers in Research Fund (NFRF), [NFRFE-2022-00159 ,] for their financial support for myself and my R.D.

Yen Hsi-Wei, for providing us with moment 0 ALMA HCO^+ data from Yen et al. (2019).

Karl Stapelfeldt, for directing us to the 2004 HST data from PID9862.

This paper makes use of the following ALMA data: ADS/JAO.ALMA#2011.0.01234.S. ALMA is a partnership of ESO (representing its member states), NSF (USA) and NINS (Japan), together with NRC (Canada), MOST and ASIAA (Taiwan), and KASI (Republic of Korea), in cooperation with the Republic of Chile. The Joint ALMA Observatory is operated by ESO, auI/NRAO and NAOJ. Some of the data presented in this article were obtained from the Mikulski Archive for Space Telescopes (MAST) at the Space Telescope Science Institute.

Dedication

I dedicate this thesis to my parents who have endlessly supported this dream of mine since I first picked up the scholastics book series on our planets by Christine Taylor-Buttler and Melanie Chrismer. These began a life long fascination with space; planets specifically. Though my path to perusing a degree in astronomy had many hurdles and moments along the road where it didn't seem possible, I was always encouraged to keep trying and to make this dream a reality; for that I am forever grateful.

Chapter 1

Introduction and Background

1.1 Overview

4.5 billion years ago, a small, rocky, planet was formed the ideal distance from its star to have liquid water, with all the correct ingredients for life to evolve: Earth. Life as we know it can only begin on a planet under a specific set of conditions, some of which are determined as the planet is forming. Though we don't have the ability to go back in time and watch the birth of our solar system, the night sky provides a window back in time, where we can watch the birth of other planetary systems around other sun-like stars. Through observing how other planets come to be, we can begin to understand ourselves.

Forming planets – called protoplanets – are forged around young stellar objects (YSOs) in regions of dust and gas known as protoplanetary disks (Williams & Cieza, 2011). To determine how the swirling cloud of dust and gas remaining from the star's formation process eventually evolves into a neat solar system with perfectly ordered planets, we must uncover the steps in-between spanning millions of years. The first stages of a planet's life are crucial; defining the eventual size, composition, and radial separation of the planet from its star, and most importantly, whether or not it could harbour life. Forming planets are directly impacted by their host disk. The elements that are accessible, whether water is present, and if the disk is isolated or connected to another system via streams of material, all affect the composition of the disk's eventual planets.

There are several fundamental concepts which must be covered to fully understand the field of planetary formation, and the constraints astronomers face to answer the fundamental questions. To better understand the research outlined in the body of this thesis, I will first walk through the crucial information needed to fully grasp these concepts, starting from the accepted mechanisms of planet formation (section 1.2), where astronomers look for protoplanets (section 1.3), how protoplanetary disks are observed (section 1.4), and lastly our

protoplanetray disk of interest: HL Tau (section 1.5). My hope is that this introduction will help highlight the significance of this work and the questions that still need to be answered.

Let us begin.

1.2 Planet Formation Mechanisms

Though the exact processes involved in planet formation are not yet fully understood, steps can be inferred through a combination of simulations and observations. The first stage of planetary growth is planetesimal formation. The dust in a disk will initially be well distributed within the gas, but will begin to settle towards the disk midplane over time where particles will collide and coagulate. Through radial drift (Weidenschilling, 1977), and streaming instability (Youdin & Goodman, 2005), the density of dust particles in the midplane will increase. This dense layer of particles will become gravitationally unstable and collapse into 100m–1km sized objects known as planetesimals (Goldreich & Ward, 1973). This first stage is thought to take no more than 100,000 years.

The next stage is the formation of terrestrial (rocky) planets. This begins with planetesimal-driven growth, where planetesimals will begin to have sufficient mass to gravitationally attract surrounding material, collide, and accrete said material until a planetary embryo is formed (Armitage, 2020). The leading theorized process for this based on observation is called pebble accretion (Ormel & Klahr, 2010; Bitsch et al., 2015; Johansen & Lambrechts, 2017; Ormel et al., 2021). In this regime, small dust particles coupled with the gas escape accretion onto the growing planetesimal and remain free floating in the disk, while larger objects will collide and accrete only if they experience sufficient gravitational and aerodynamic forces (Ormel & Klahr, 2010). The largest planetesimals will accrete smaller pebbles the fastest, leading to runaway pebble accretion (Safranov & Ziglina, 1991; Lambrechts & Johansen, 2012). A planetary core or protoplanet is formed once sufficient mass is accreted. The rate of accretion onto the planetary embryo before disk dissipation is a limiting factor in how large a protoplanet can become (Pollack et al., 1996; Rafikov, 2004; Bitsch et al., 2015).

Giant planets generally have a substantial gaseous envelope, thus earning the name “gas giants”. There are two proposed formation pathways for giant plants: “hot start” (Boss, 1997; Marley et al., 2007) and “cold start” (Baraffe et al., 2003). These stem from two competing theories of formation: disk instability and core accretion. In the instability scenario, the protoplanetary disk becomes locally gravitationally unstable and collapses to directly form a giant planet (Boss, 1997). The gas from the disk that collapsed to form the planet

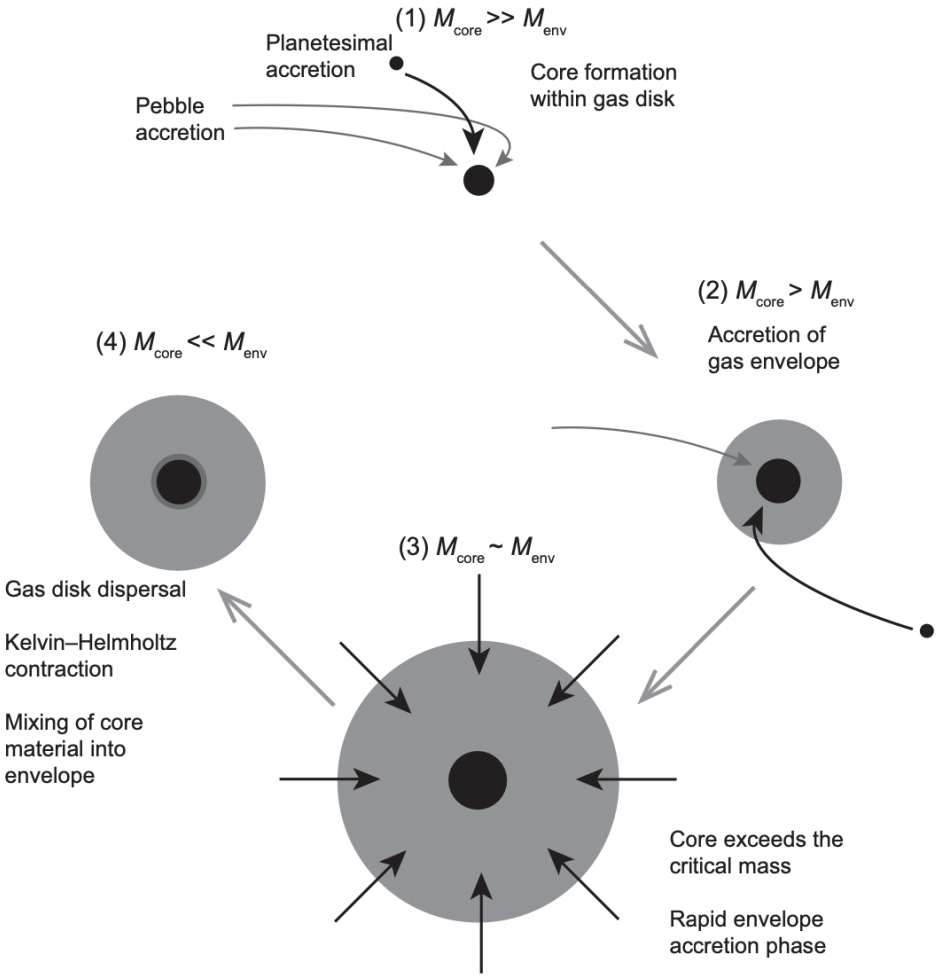

Figure 1.1: The stages of giant planet formation using the core accretion model. Once the solid planetary core is formed via pebble accretion, it will begin to accrete gas forming an atmosphere, and eventually stabilizing. Credit: Armitage (2020)

will retain most of its entropy, resulting in the planet having high initial entropy (i.e. a "hot start"). Core accretion – as illustrated in Figure 1.1 – begins with the formation of a solid planetary core via planetesimal collisions and pebble accretion. Once the thermal velocity of the gas surrounding the planetary core has dropped below the core's escape velocity, the protoplanet will begin to accrete gas from the disk to form an envelope or atmosphere (Emsenhuber et al., 2021). The core and envelope will grow until the core exceeds a critical mass and will begin rapid "runaway" gas accretion (Pollack et al., 1996). The accretion process cools the gas, causing it to lose most of its entropy, thus forming a planet with low initial entropy (i.e. a "cold start"). While hot-start planets are generally predicted as having larger radii and higher effective temperature than cold-start ones, in reality planets formed

by either mechanism could have overlap in properties leading to the often favoured "warm start" scenario (Spiegel & Burrows, 2012).

Giant planets formed via disk instability are thought to have solar levels of element abundance, while core accreted planets could contain heavier elements (Matsuo et al., 2007). Most gas-giant planets have been found to have heavier elements. Therefore, the core accretion model provides the best explanation for the formation of most giant planets (Matsuo et al., 2007; Mordasini et al., 2012). Thus, core accretion is likely the process behind the formation of the giant planets which are detectable in protoplanetary disks. Though this process cannot be observed for a single planet from beginning to end, each step can be confirmed by detecting planets at different stages of formation.

1.3 Signposts of Planets

Forming planets are exceedingly difficult to detect, but their presence can be inferred through indirect detection. The act of a protoplanet accreting dust and gas from its disk leaves observable traces, such as gravitational alterations to disk morphology, or accretion line emission. It's these signposts of planet formation that observational astronomers use as a guide when looking for young planets. While we cannot determine specific planet characteristics from this, it can help with locating a planet.

1.3.1 Disk Morphology

Protoplanetary disks are not simply flat, morphologically homogeneous, disks of matter surrounding young stars. They often harbour notable substructures such as rings and gaps (e.g. HL Tau ALMA Partnership et al. (2015)), spiral arms (e.g. MWC 758 Benisty et al. (2015), or large cavities (e.g. PDS 70 Müller et al. (2018)). Examples of the range of disk morphologies can be seen in Figure 1.2. Various mechanisms have been proposed to explain how these large-scale features appear; the most enticing pointing to planet-disk interactions. The variety seen in protoplanetary disk morphology may be due to the unique and complex interactions between each forming planet and its host disk. If planets are the cause of disk substructures, then substructures can be used as an indicator for which disks to target when looking for planets, and a marker for where in the disk planets are expected to be.

This work focuses on the disk HL Tau, which has many solar-system scale rings and gaps, as shown in Figure 1.2. Some ring and gap disks only contain a simple inner ring and outer ring of dust separated by a large gap, several astronomical units (au) in width, while other disks have multiple rings with more narrow gaps separating them. Rings and gaps are the

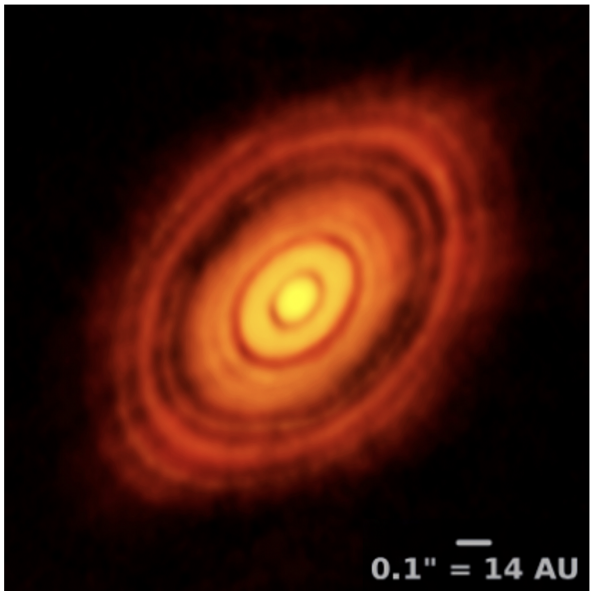

(a) Rings and Gaps

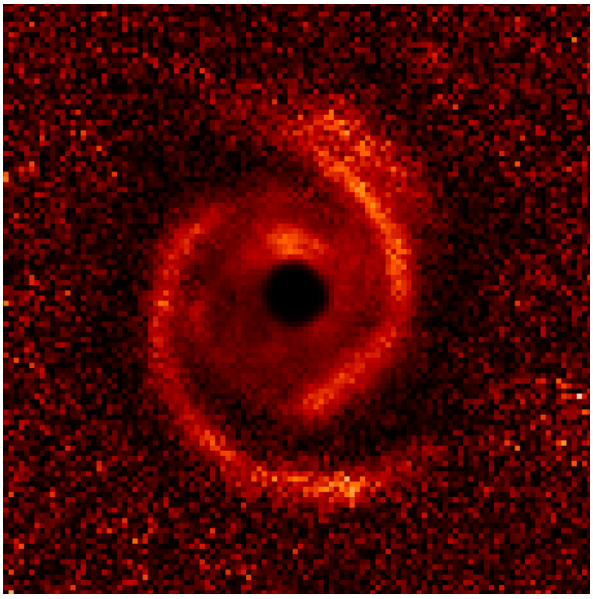

(b) Spirals

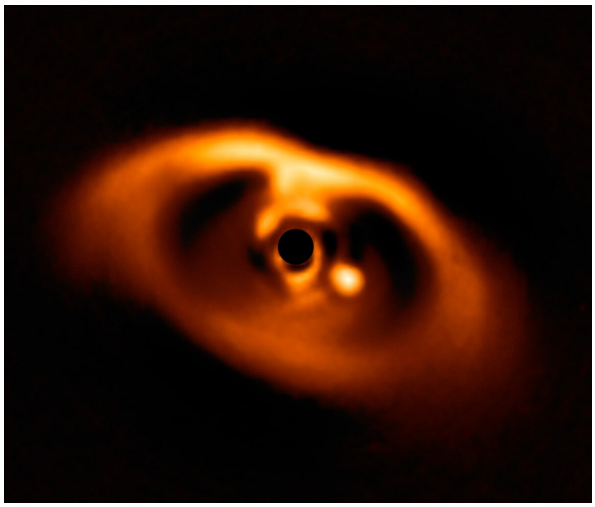

(c) Large Cavity

Figure 1.2: 3 common categories of protoplanetary disk morphology: (a) rings and gaps as shown here with HL Tau at 1.33mm (ALMA Partnership et al., 2015), (b) spiral arms as shown here with MWC 758 at 1.04μm taken within 0.53″ (148 au) (Benisty et al., 2015), (c) a large cavity opened by planets as shown here with PDS70 at $2.1 - 2.5\mu$m within 1″ (113 au) (Müller et al., 2018).

most commonly found substructures in protoplanetary disks (van der Marel et al., 2019), and the simplest conceptually as an indicator for planets. A planet orbiting a star within a disk can clear a gap in its orbital path. A gas pressure bump will form on the outer edge of the planet-induced gap. While dust orbits the star at Keplerian velocity, gas orbital speed is affected by the pressure gradient. Dust particles will experience a headwind or tailwind from the gas and therefore lose or gain angular momentum, which can cause them to drift radially towards gas pressure maxima (Zhu et al., 2012; Armitage, 2020). As a result, the pressure bump caused by the gap-opening planet acts as a barrier for inward drifting dust, resulting in a dust ring forming outside the gap (Pinilla et al., 2012; Zhu et al., 2012; Pinilla et al., 2015; Long et al., 2018). Since dust cannot flow through the gap (unlike gas), the dust in the gap will be depleted; this process is called "dust filtration" (Rice et al., 2006). This suggests forming planets can be the cause of disk gaps, and if a gap is present in a disk, there is likely a planet there. The size of a gap, and number of gaps, in a disk could indicate the number of planets forming in a system, and the size of the planet within each gap; though this is not always a direct correlation (Dong et al., 2017, 2018; Lodato et al., 2019). Gap size could also potentially indicate planetary age (Helled et al., 2014); for younger systems, the planet will not have accreted sufficient material to create a wide gap and thus the disk will have shallower, narrower, gaps containing more material for the planet(s) to accrete.

While these theories are intuitively sound and replicable with disk simulations, it is rare to actually observe a planet within a disk gap. Whether this is a matter of inadequate instrumentation, or a fault with the theory, is a longer discussion without a current conclusion. In recent years, various mechanisms other than planet-disk interaction have been proposed to explain the presence of rings/gaps in disks. Some examples include instability from gas-dust friction (e.g. Takahashi & Inutsuka, 2014), mean-motion resonance (e.g. Boley, 2017), self-induced dust traps causing a pressure maxima (e.g. Gonzalez et al., 2017), and Rosbey-Wave instability triggered through envelope infall (e.g. Bae et al., 2015). It is possible these other mechanisms explain a large percentage of observed ring and gap disks considering how uncommon planet detections are. Out of hundreds of disk observations, the number of confirmed planet detections within a disk are limited to PDS 70 b and c (Keppler et al. (2018); Müller et al. (2018)), AB Aur b (Currie et al. (2022)), and HD 169142 b (Hammond et al. (2023); Reggiani et al. (2014)); with HD 169142 being the only ring and gap disk. Though troubling, this does not disprove planet formation as a mechanism for gap opening. Rings and gaps will continue to be treated as an indicator for planets until such a time as this link is disproved, or proven too rare. As such, the program I am a part of targeted two disks that have rings and gaps with the hopes of detecting gap-opening planets, and pushing the

limits of detection.

1.3.2 Accretion Signatures

The growth of a planetary core into a gas giant relies on the planet's ability to radiate accretion energy (Pollack et al., 1996). This accretion energy can be used as an indication for planet formation within a disk. Observationally, accretion in a disk is recognized through detection of hydrogen (H) emission lines. The Hα line occurs when accretion shock heating causes hydrogen to be heated to tens of thousands of degree kelvin (Aoyama et al., 2018; Mordasini et al., 2012). Accretion onto large gas-giant planets can produce accretion shocks that are traceable through line emission. In this scenario, accretion shocks would arise on the surface of the young planet as it accretes gas from the disk into its atmosphere (Mordasini et al., 2012). The tracing of these shocks can help indicate where a planet could be interacting with a disk (even if the planet itself is not visible), and the rate of accretion can help indicate the rate at which the planet is actively growing. Accretion is not only traceable through Hα, but is also detectable through the emission of other lines such as Lyman(Ly)-α, Paschen(Pa)-α and Brackett(Br)-α. In scenarios where a protoplanet cannot be directly detected, localized accretion signatures within a disk are a hopeful sign that a planet is present but has escaped direct detection.

1.4 Observing Disks

1.4.1 Instruments and Wavelength

Though astronomers have access to observing instruments that operate in wavelengths ranging from x-ray to radio, near-infrared (IR) to mid-IR wavelengths are often favoured for detecting protoplanets. IR is ideal for detecting objects that are low temperature and do not emit much visible light, but still radiate thermal emissions. Young planets are feeble energy sources when compared to a star, and do not emit their own visible light, but will radiate thermal energy remaining from their formation process. Protoplanets are thus "brighter" in the IR than in visible light, and therefore easier to detect. A young planet embedded in a disk will be shielded by disk dust and gas that deflects visible light's short wavelengths, further complicating a detection with an optical telescope. Conversely, IR wavelengths are longer and lower energy and thus can escape a dust field, making otherwise shielded planets visible through IR instruments. Though one might suggest going even longer into the sub-mm or radio wavelengths, the best detection range for young planets is around the crossover be-

tween NIR and MIR wavelengths ($\sim 2\mu\text{m} - 6\mu\text{m}$) where dusty disks become less opaque and young planets' thermal emissions peak. Beyond this, the advantage of tracing the planets' thermal emissions is lost, as we move into the radio where colder gas and dust are traced.

Making observations of young planets in disks is crucial to testing planetary formation theories. However, mid-IR observations are challenging from the ground. For decades, astronomers accessed the IR with ground-based telescopes such as the Infrared Telescope Facility (IRTF), Canada-France-Hawaii Telescope (CFHT), Subaru telescope, and Very Large Telescope (VLT). However, ground-based observations are affected by weather patterns, cloud cover, and atmospheric turbulence, as well as mid and far-IR wavelengths being absorbed or blocked by Earth's atmosphere. The invention of space telescopes such as the Hubble Space Telescope (HST), provided an unobstructed view for astronomers and access to new wavelengths. Space telescopes also provide longer observational windows, since observations can be carried out during daytime on Earth. Hubble observes at ultraviolet, visible, and NIR wavelengths, but does not have access to longer wavelengths. Now, as of December 2021, the James Webb Space Telescope (JWST) provides an unprecedented opportunity to push the limits of detection in the NIR and MIR. With its increased sensitivity compared to ground based instruments, JWST is expected to increase the number of detected protoplanets and further the understanding of planetary formation (Green et al., 2005; Girard et al., 2022; Rieke et al., 2023). This impressive new telescope's Near-Infrared Camera (NIRCam) ($0.6\mu\text{m} - 5\mu\text{m}$) is the instrument used in this research. JWST is a leap-forward in capabilities compared to past space telescopes such as HST ($0.8\mu m - 2.5\mu m$), Spitzer Space Telescope ($3.6\mu m - 160\mu m$), Herschel Space Observatory ($55\mu m - 672\mu m$), and the Infrared Astronomical Satellite (IRAS) ($8\mu m - 120\mu m$). In the wavelength range that these facilities overlap, JWST dominates. A primary difference is the size of the primary mirror. JWST's primary mirror is 6.5m, as compared with the Herschel's 3.5m mirror which was the largest IR space telescope before JWST. Subsequently, the angular resolution ($0\farcs07$ at $2\mu m$) is also notably improved when compared with the past IR space telescopes: $0\farcs5$ for IRAS and $2''$ for Spitzer. These improvements allow JWST to image objects which are fainter and closer in separation than its predecessors.

1.4.2 Isolating Planet Signal

A crucial part of designing an observation is ensuring the ability to extract the desired signal within the data. Simply pointing an IR telescope in the direction of a protoplanetary disk will not yield the desired results of a disk and/or planet detection. When searching for

planets, the greatest challenge is contrast. The IR light emitted by a planet is several orders of magnitude fainter than the light emitted by its host star. In order to detect planets – whether fully formed or in the formation stages – this star light must be removed from the observed images. There are several standard techniques used to remove star light when searching for forming planets in a disk. Some take place during the observation, and some are implemented afterwards. During an observation, the star light can be blocked using a coronagraph; a mask placed in the center of the detector to block direct light from the star, while planet light comes in at an angle, bypassing the mask.

After the observations are taken, the star must be removed with techniques after observations. The three most commonly used techniques are angular differential imaging (ADI), reference star differential imaging (RDI), and polarimetric differential imaging (PDI). As the name would suggest, PDI uses polarized light, capitalizing on the fact that stellar light is un-polarized, but light scattering off of dust grains in a disk will be polarized (Kuhn et al., 2001). Similarly, planets can also be polarized at NIR wavelengths from their thermal emission being scattered by particles in their outer atmospheres or by dust particles surrounding them (Sengupta & Marley, 2010; Stolker et al., 2017; de Boer et al., 2020). This allows the observer to filter out un-polarized light from the images, thus removing the star while preserving the disk and planet light. ADI and RDI don't require polarized light and are generally performed with total intensity data; they are also the two techniques which were explored in this work. ADI removes the stellar point spread function (PSF) by capitalizing on the fact it will remain unchanged with rotation (Schneider et al., 1998; Heap et al., 2000; Marois et al., 2006). If the angle of the observing instrument is changed by rotating the telescope, then the PSF will have the same orientation but the orientation of the image will have shifted. In its simplest form, ADI can be performed with two images if they have a significant enough angular difference between them. If there is a planet in the data, then its position in the image will have shifted between the two images due to the telescope rotation, allowing one image to be subtracted from the other to remove the identical PSF while keeping the planet signal intact. The two images are then rotated to align with one another leaving a residual image with one or more clear planets now that the stellar PSF is removed.

Though ADI is a simplistic but effective technique, its effectiveness diminishes when working with extended structures. Any object present in the de-rotated residual images will have negative side lobes as a result of over subtraction between the background and the bright object in another image. This is not a problem when dealing with a simple star and planet system, where the side lobes don't distort its point-source shape. However, once an extended disk or stellar envelope are present in the data, the negative side-lobes can

greatly distort the final image with large negative spaces that make the image difficult to analyze. In such a scenario, RDI can be a more effective technique. RDI removes the stellar PSF by finding a match to the star's spectral energy distribution (SED) in another star and subtracting that reference star from the target star (Lafrenière et al., 2009). Ideally, this PSF reference will not contain a disk or planets of its own so that the residuals are uncontaminated. If an ideal match is found, the light from the target star can be subtracted with a simple frame subtraction, and the light from any disk or planets (not present in the reference PSF) will remain intact. Though RDI is an effective technique, it can be challenging to find an adequate reference star for every target. In the case of complex systems with large extended structures that modify the PSF, reference stars may not adequately mimic the PSF. When real stars are insufficient as a reference, observers sometimes turn to software to create synthetic PSF matches as a way of mimicking the RDI technique without needing to find and observe another star.

1.5 HL Tau

This thesis focuses on the protoplanetary disk surrounding the Class I T-Tauri star HL Tauri (HL Tau), located in the Taurus star forming region 140 pc away. The HL Tau disk is still embedded in a stellar envelope, as is typical for a system of its age (∼0.1 Myr; Stephens et al. 2017). The envelope environment has been shown to have several active features such as an outflow/cavity and in-flowing streamers which could be associated with accreting material from the envelope to the disk (e.g., Garufi et al., 2022). Long-baseline interfermotric observations with the Atacama Large Millimeter/Submillimeter Array (ALMA) revealed the disk around HL Tau to have multiple rings and gaps at solar system scales as seen in Figure 1.2 (ALMA Partnership et al., 2015). It is theorized that these gaps were formed by interactions between the disk and one or more young planets via gravitational perturbations (e.g., Paardekooper et al., 2022). Dong et al. (2015), Dipierro et al. (2015) and Jin et al. (2016) have suggested that each of the three major gaps (12 au, 30 au, and 65-75 au) could be opened by a ∼Saturn mass planet. Dong et al. (2018) proposed that a sub-Saturn mass planet at ∼71 au could produce all three gaps if the disk viscosity is sufficiently low. As of writing this thesis, no planets have been observed in the disk to confirm these theories. Due to its young age as compared to most other observed protoplanetary disks, HL Tau remains a primary target in the hopes of finding the youngest planets observed to date. I have now joined this long history of observers, using JWST/NIRCam to observe HL Tau, where the findings of this observation are presented in this work.

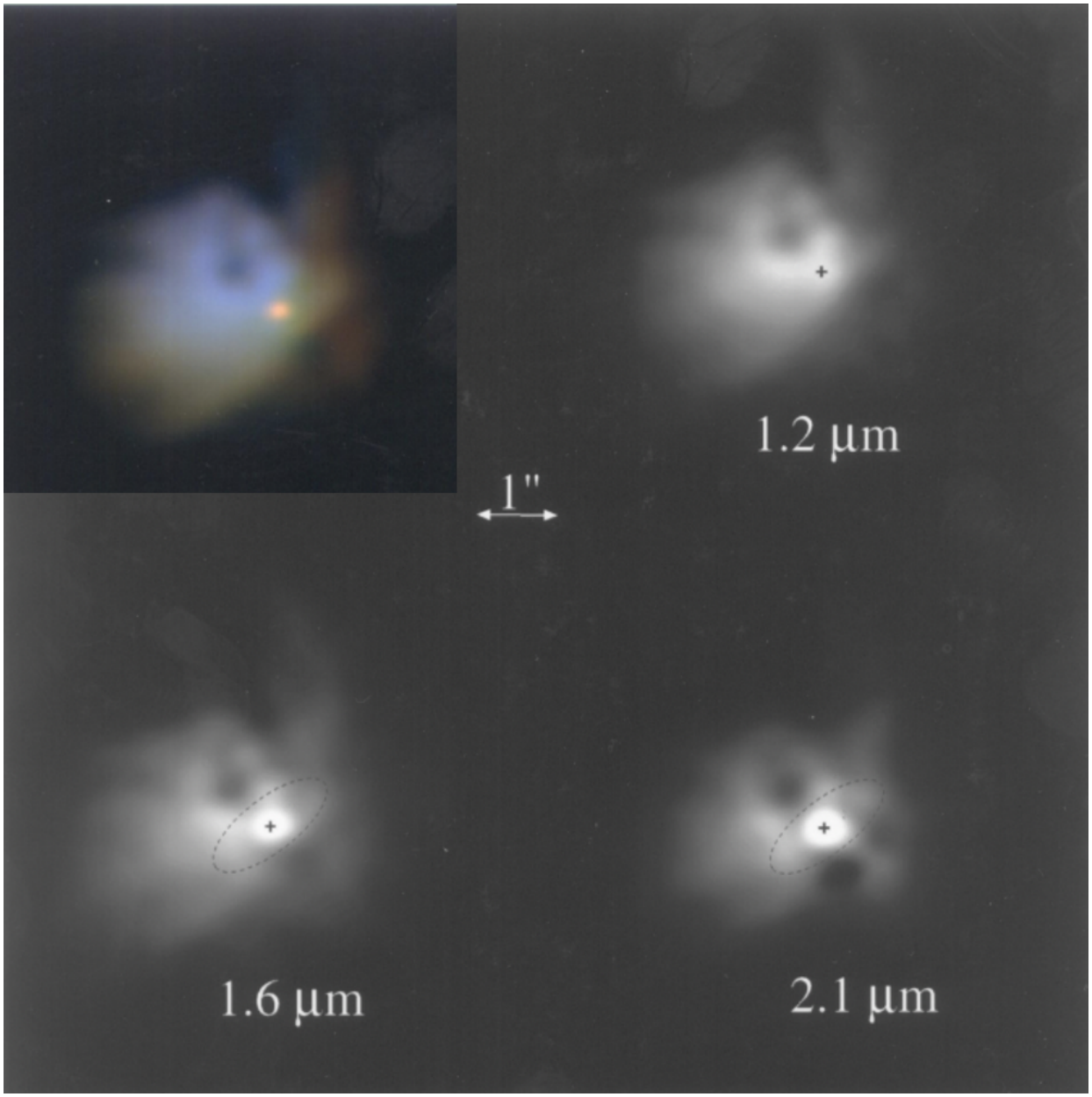

Figure 1.3: Main findings from Close et al. (1997) showing observations of HL Tau. The grey-scale images show the CFHT observations at increasing wavelength and the RGB image in the upper left corner shows an overlay of the three panels. Blue is from the Stapelfeldt et al. (1995) HST observation and the 1.2μm CFHT filter, green is the 1.6μm filter, and red is the 2.1μm filter.

Table 1.1: Key Parameters of HL Tau and its Disk

Parameter	Value	Reference
RA (J2000)	04:31:38.425	1
DEC (J2000)	+18:13:57.242	1
Distance [pc]	140	2
Age [Myr]	0.1	4
$M_\star$ [$M_\odot$]	1.3	1
Spectral Type	K5 $\pm$ 1	3
disk i [°]	46.72 $\pm$ 0.05	1
disk PA [°]	138.02 $\pm$ 0.07	1

References: (1) ALMA Partnership et al. (2015). (2)Rebull et al. (2004). (3) White & Hillenbrand (2004). (4) Stephens et al. (2017).

1.5.1 Summary of Past Observations

Numerous studies of HL Tau have observed its surrounding environment using a variety of instruments ranging from the optical, through the IR, and into sub-mm/mm wavelengths. Here, I present a summary of relevant past observations to lay the groundwork for the new research I hope to accomplish. Key parameters of HL Tau and its disk are listed in Table 1.1.

Before its famous disk was discovered, and HL Tau was thought to be just a young star, early images – taken with the 2.2 m telescope at the Calar Alto Observatory and IRTF – revealed that HL Tau was surrounded by a $\sim$20″ cloud of gas (Mundt & Fried, 1983; Grasdalen et al., 1984). Mundt & Fried (1983) discovered an ionized jet originating from HL Tau, extending northeast (NE) at a position angle of 36°. Cohen (1983) observed an excess in the IR surrounding the star, which Grasdalen et al. (1984) hypothesized could result from the re-radiation of starlight absorbed by dust grains in a protoplanetary disk. Stapelfeldt et al. (1995) used the HST to image HL Tau at optical wavelengths, revealing the previously mentioned jet and structures known as Herbig-Haro objects, providing a glimpse of the active environment surrounding the young star. Close et al. (1997) imaged HL Tau using CFHT, where the data showed similar envelope features to Stapelfeldt et al. (1995) in H′, J, and K bands, as well as evidence for an active accretion disk with bipolar cavities; the main findings from those observations are are shown in Figure 1.3. The variance of envelope morphology with wavelength is evident and will be discussed in section 2.4.1. Close et al. (1997) surmised the upper and lower cavities were opened by an outflow, relating to the previously observed jet. Murakawa et al. (2008) imaged HL Tau using the adaptive optics

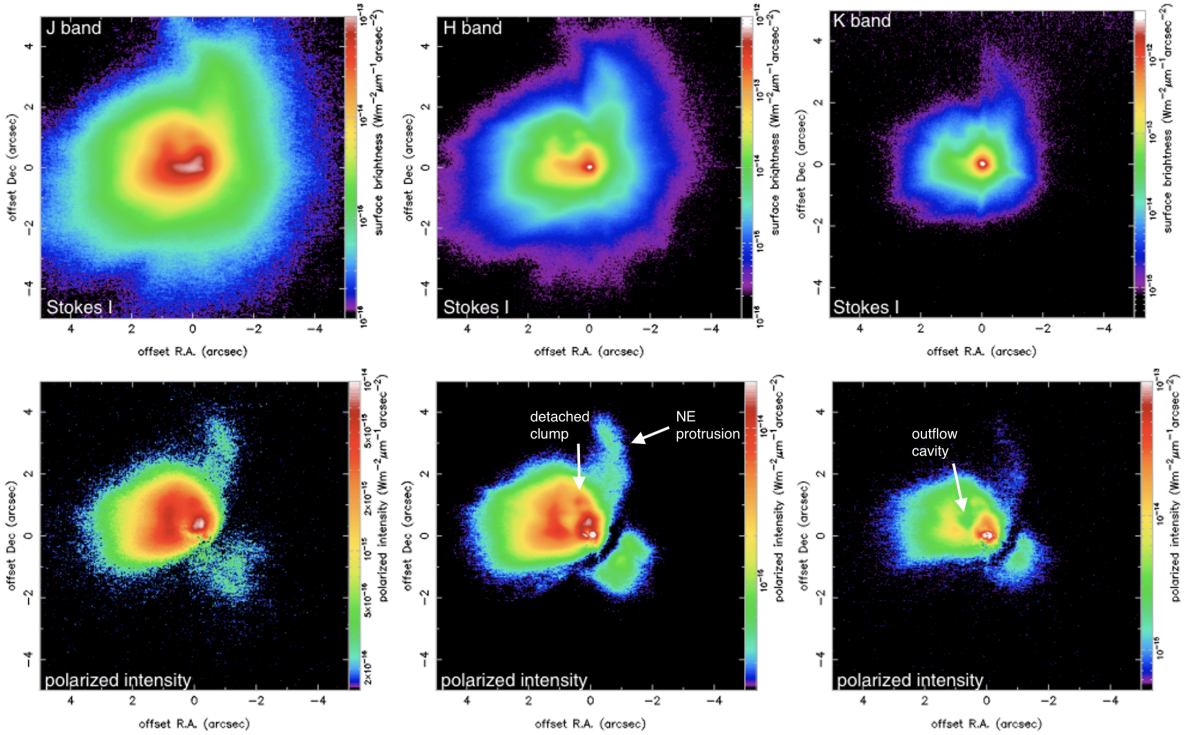

Figure 1.4: Annotated results from Figure 1 of Murakawa et al. (2008) showing HL Tau in IR total intensity and polarized intensity light. A NE protrusion from a streamer, and outflow cavity are visible. The detached clump will be discussed in section 2.4.1.

equipped NIR camera CIAO on Subaru, revealing a "butterfly-shaped" polarization disk and extended envelope structure out to 4″ with a north facing extended feature highlighted in Figure 1.4. HL Tau's active envelope was apparent – we'd never seen through to the disk.

A new era of observing for this target began with the ALMA Partnership et al. (2015) Long Baseline Campaign, which provided the clearest images of HL Tau's disk structure to date, revealing multiple solar-system scale rings and gaps at mm wavelengths – see Figure 1.2. These features were regarded as striking evidence for planets in a protoplanetary disk, and began the planet hunting focus for this target. Yen et al. (2019) used ALMA to study HCO^+ emission from HL Tau and found a gas gap at 30 au consistent with being opened by a planet of 0.5-0.8 Jupiter masses (M_J), using the gap depth *vs* planet mass formula in Kanagawa et al. (2015). In addition, Yen et al. (2019) detected a one-arm spiral in HCO^+emission, ∼530 au in length extending from disk midplane and originating from an in-falling streamer. This same streamer is drawn in red in Figure 1.5. Garufi et al. (2021, 2022) studied the disk-outflow with ALMA, finding SO and SO_2 molecules spiraling towards the star. Garufi et al. (2022) found a blueshifted infalling component in the NE direction,

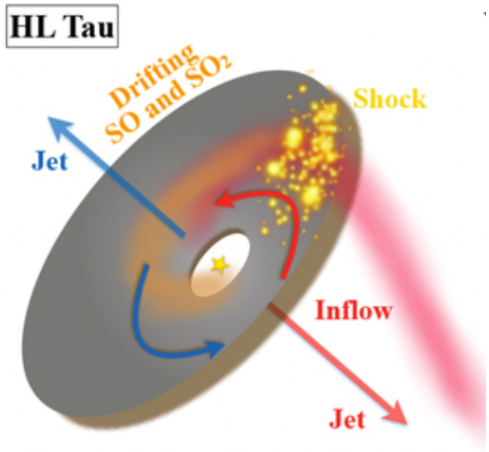

Figure 1.5: Graphic from Figure 7 of Garufi et al. (2022). This shows how the intersection of the red colored in-flowing streamer with the grey disk correlates to the yellow accretion shocks as traced by SO and SO_2 molecules.

a redshifted infalling component in the SW direction, and a NW redshifted component associated with a streamer. From this, Garufi et al. (2022) determined that the presence of SO and SO_2 molecules could be used to probe accretion shocks in the disk, since those molecules corresponded to intersections between the disk and in-flowing streamers, as is displayed in Figure 1.5.

The HL Tau disk has also been studied in the IR from the ground prior to JWST. Testi et al. (2015) used the Large Binocular Telescope Interferometer (LBTI) Long-Mid IR Camera (LMIRCam) (Leisenring et al., 2012) to search for giant planets in HL Tau's outer 64 au and 73 au gaps. Testi et al. (2015) took L′ (∼3.8 μm) and K (∼2.2 μm) band images, finding that the scattered light from the envelope impacted their ability to search for planets – especially in K band. Their main PSF subtraction results can be seen in Figure 1.6, where envelope signal is apparent by the white positive signal shown clearly in the left pannel and faintly on the right. With an inner masked region of 0.″18, Testi et al. (2015) did not detect any companion candidates in their images. The L′ NaCo-ISPY survey (Cugno et al., 2023) also imaged HL Tau, but no companions were detected in the system. With all past observations failing to detect planets in this disk, observers turned to the newest and best facility – JWST – to try again.

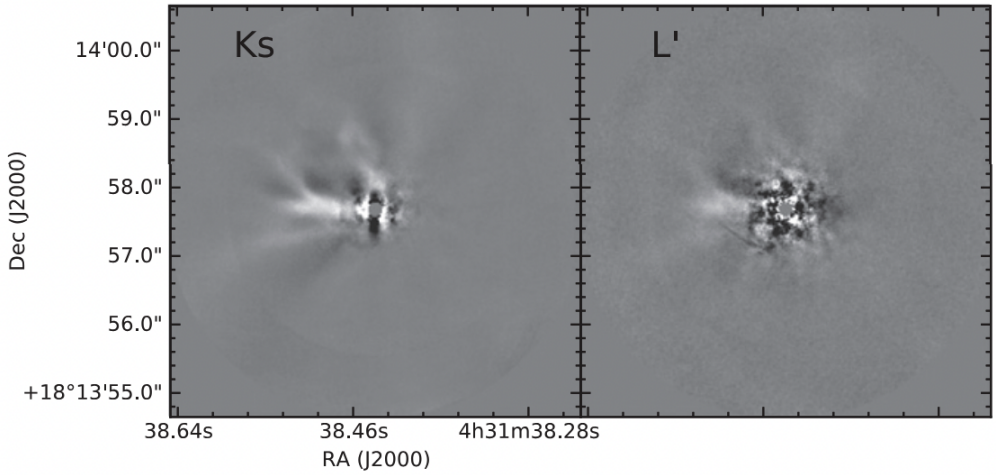

Figure 1.6: ADI PSF subtractions from Testi et al. (2015). The K-band images show some minor envelope structure while L-band have nearly completely subtracted the envelope.

Chapter 2

Project

2.1 Research outline

This work has already been peer reviewed and published in the Astronomical Journal as Mullin et al. (2024). Though I was the lead author on the paper, I value the contributions and feedback from my collaborators, and this would not have been possible without their support and contribution. As part of the JWST Guaranteed Time Observation (GTO) program "Direct Imaging of YSOs" (program ID 1179), I performed high contrast imaging on one of the first planetary formation environments to be observed by NIRCam. HL Tau was chosen to test NIRCam's capabilities for imaging YSO environments, due to a long history of past observations that provide compelling evidence for ongoing planet formation processes in its protoplanetary disk. NIRCam's superior sensitivity and imaging quality in the IR have produced images of the disk's surrounding envelope in unprecedented detail, allowing me to probe these regions for possible companions. In this work, I searched for planets both inside and outside the ALMA disk region and set constraints on planet detection limits.

This chapter is organized as follows. In section 2.2, I break down how I took observations and my data reduction methods. In section 2.3 I show results and in section 2.4 I discuss them. My summary and conclusions are found later in section 3.1.

Table 2.1: Summary of Observations

Target	Prog. ID	Filter	$\lambda_{\rm mean}$ (μm)	$\rm W_{eff}$ (μm)	Readout	SUB	$N_{\rm gr}$	$N_{\rm int}$	$N_{\rm dither}$	$N_{\rm roll}$	$t_{\rm tot}$ (s)	FWHM ($''$)
HL Tau	1179	F187N	1.874	0.024	RAPID	SUB160	10	120	4	2	2680	$0\farcs064$
HL Tau	1179	F200W	1.990	0.461	RAPID	SUB160	10	120	4	2	2680	$0\farcs066$
HL Tau	1179	F405N	4.055	0.046	RAPID	SUB160	10	120	4	2	2680	$0\farcs136$
HL Tau	1179	F410M	4.092	0.436	RAPID	SUB160	10	120	4	2	2680	$0\farcs137$
Injected Point Source												
P330-E	1538	F187N	1.874	0.024	RAPID	SUB160	7	2	4	1	15.6	$0\farcs064$
P330-E	1538	F200W	1.990	0.461	RAPID	SUB160	3	2	4	1	6.7	$0\farcs066$
P330-E	1538	F405N	4.055	0.046	RAPID	SUB160	10	2	4	1	22.3	$0\farcs136$
P330-E	1538	F410M	4.092	0.436	RAPID	SUB160	3	2	4	1	6.7	$0\farcs137$

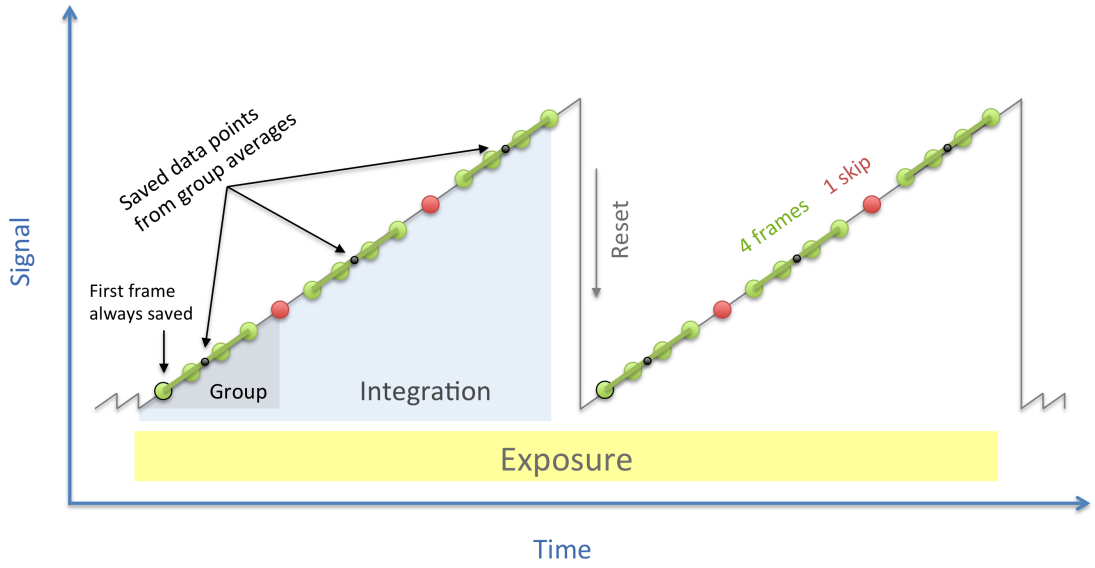

Figure 2.1: Graphic from the JWST documentation showing NIRCam Detector Readout Patterns. The green circles represent the frames to be averaged, while the red ones are skipped/discarded frames. Each sequence of green frames forms a group, with a maximum of 20 groups per integration. Each integration results in an image which will eventually be averaged together to obtain the final reduction.

2.2 Observations and Data Reduction

The observations of HL Tau were taken on UT 2022-09-29 with JWST/NIRCam in direct imaging (non-coronagraphic) mode as part of GTO program 1179 (see Table 2.1 for an observation summary). Direct imaging mode was used because, in pre-flight simulations, direct imaging could detect objects ~ 2 magnitudes fainter than coronagraphic observations for the same allocated time. This program observed five disks in total, the other four being MWC 758 (Wagner et al., 2024), SAO 206462 (Cugno et al., 2024), PDS 70 (Leisenring et al, in prep), and TW Hya (Wolff et al, in prep). For all observations discussed in this work, two filters were used for H line emission (F187N and F405N) and two for continuum emission at similar wavelengths (F200W and F410M). For each observing wavelength, two spacecraft roll angles were used – 10° rotational separation – to allow for ADI. Four dither positions were used per image to correct for saturated or dead pixels.

Each NIRCam exposure consists of a set of integrations. An example showcasing these exposure reads can be seen in Figure 2.1. NIRCam uses "up-the-ramp" fitting. As charge accumulates during an integration, the detectors are read out multiple times sampling the data while still conserving the charge in each pixel. Each readout pattern produces a ramp

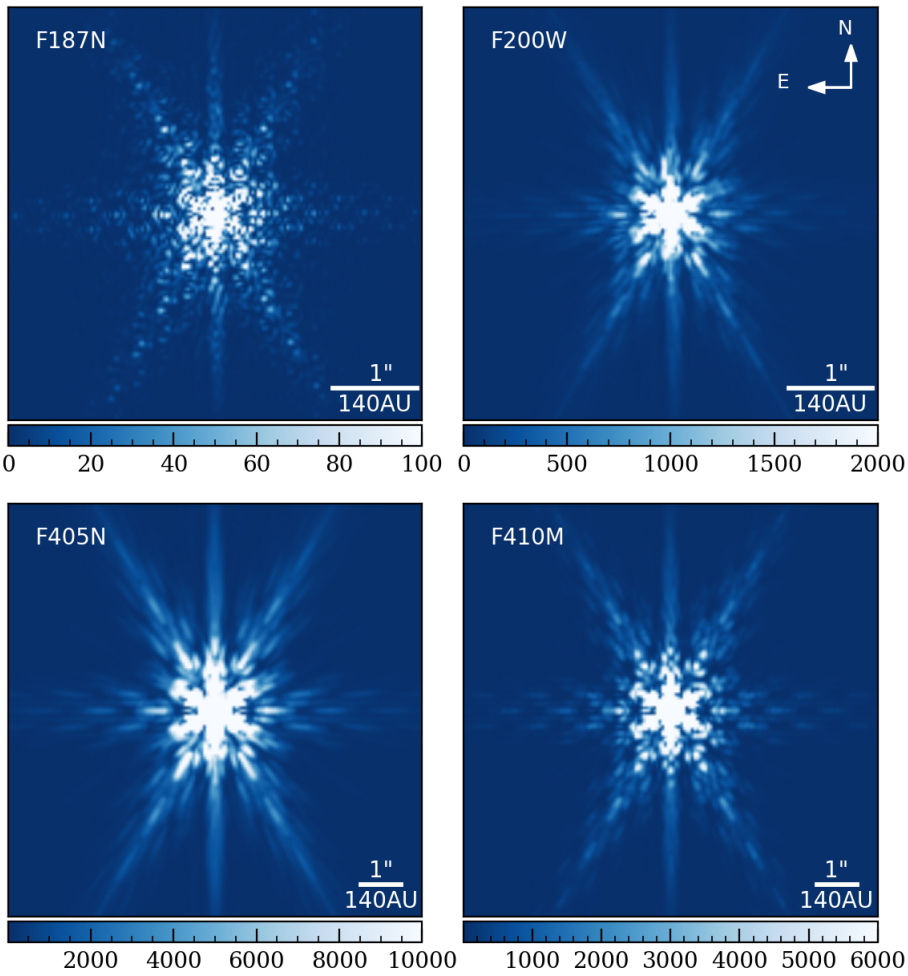

Figure 2.2: Perfect `webbpsf` for the four filters used, where color is in units of MJy/sr. This represents how the PSF should look for a perfect point source with HL Tau's photometery as viewed in each filter.

of up to 20 data points, where a data point is obtained by averaging as many as 8 frames. The combination of averaged frames is a group. The total exposure time is the photon collection duration for each dither position. For my data, all integrations consisted of 10 groups in RAPID mode, resulting in 10 non-destructive reads up each integration ramp. The observations used the SUB160P subarray, setting 480 integrations per roll position for each filter, totaling 960 image frames and an exposure time of 2680s per filter.

I reduced the data using the standard `jwst` pipeline (version 1.8.2 with crds version 11.16.15) for the initial reduction stages to obtain calibrated image files (`calints` data). Following the same process as Cugno et al. (2024), I began with the Level 1 `uncal` files and ran stage 1 of the `jwst` pipeline. Stage 1 flags bad pixels, performs reference pixel correction

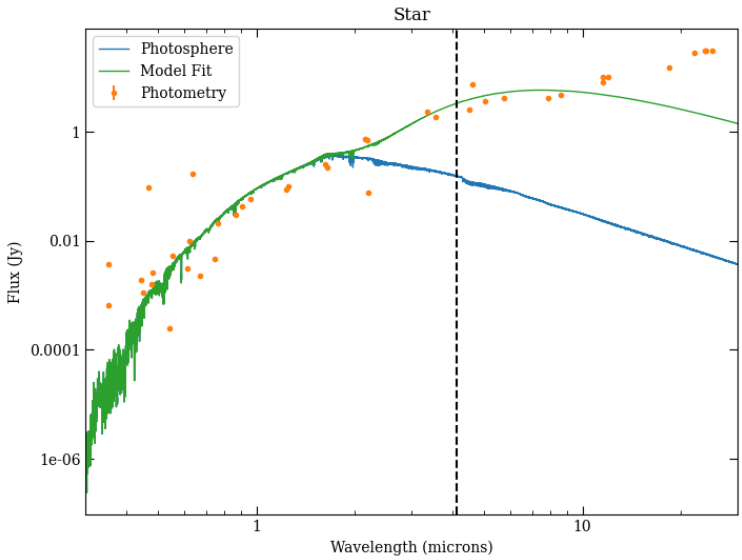

Figure 2.3: SED fit to HL Tau photometry to generate `webbpsf` for F405N. For additional SEDs, see Appendix A.

(if available), corrects for non-linearity, and fits slopes to the ramp data to create `rateints` files. I disabled the `suppress_one_group` option to obtain signal information for pixels that saturated prior to sampling of the second group. Because of poor quality of the subarray dark calibration files, I turned off dark current correction. The jump detection threshold was set to 5 as per the suggestion of Carter et al. (2023). I then ran stage 2 of the pipeline which applies flux calibration and distortion corrections during the conversion of `rateints` into `calints`. Though the JWST/NIRCam pipeline can be used for end-to-end data reduction, the unique properties of my HL Tau data required me to have more flexibility and control over each reduction step. Therefore, I opted to not continue my data reduction with the JWST/NIRCam pipeline after the calibrated data files were created.

Once the calibrated files were obtained, I completed all remaining reduction processes and analysis steps in `PynPoint` (Amara & Quanz, 2012; Stolker et al., 2019). The `PynPoint` pipeline has built-in processes for bad pixel correction, centering, synthetic PSF generation, PSF subtraction, and synthetic planet injection. To correct for bad pixels, I followed the same process as Cugno et al. (2024), by using the default bad-pixel correction code, which replaced flagged pixels with the median value of the same sky location from the other three dither positions for the given filter and roll angle. For all remaining steps, the code for the processes were written or modified by me to handle HL Tau's unique requirements.

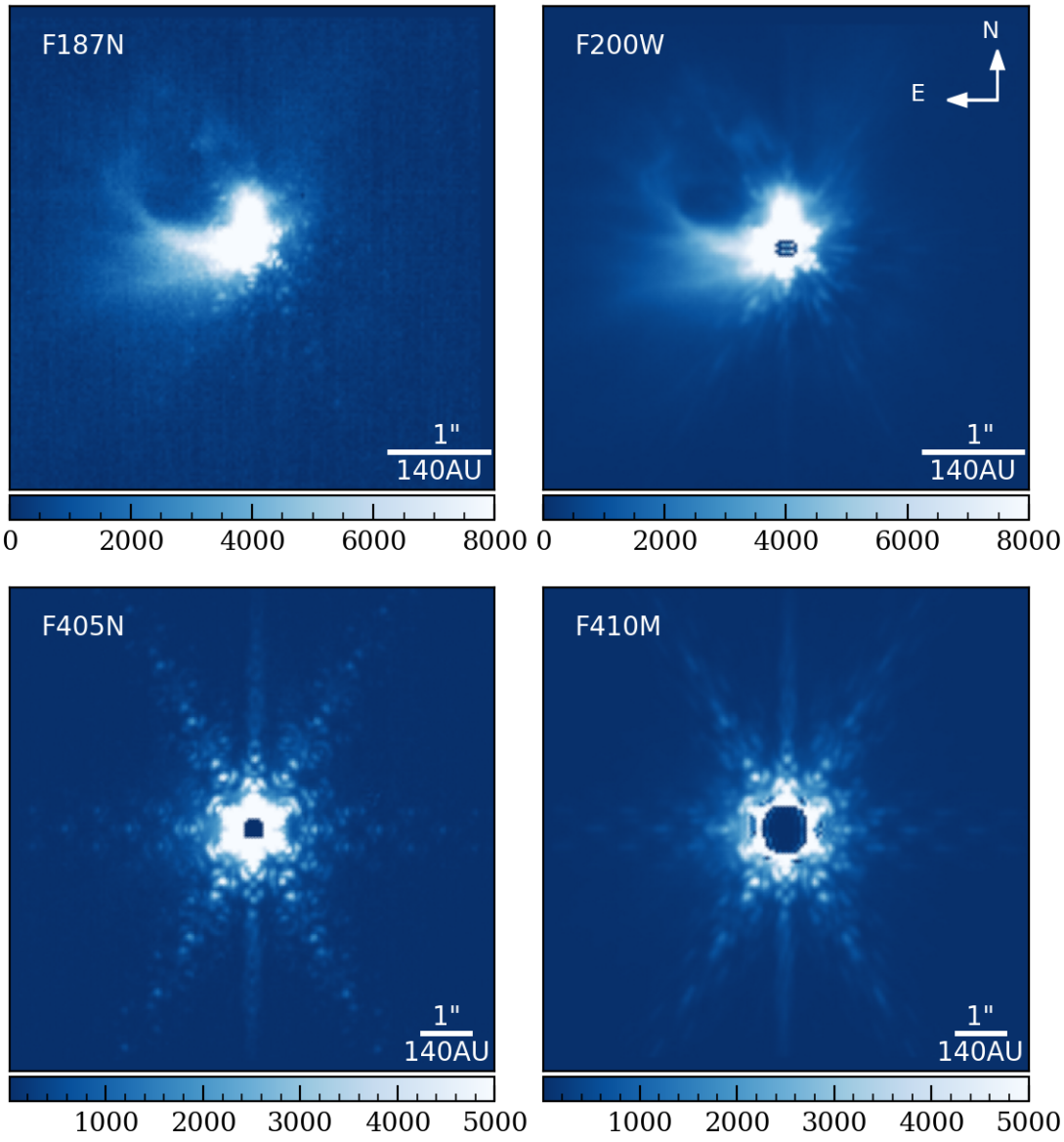

Figure 2.4: `calints` files for the four filters used where color is in units of MJy/sr. These images are centered using my code built in `PynPoint`. Despite the PSF not being removed yet, the stellar envelope is apparent at short wavelengths and is as bright as the PSF. The central saturation regions, which extend out to 0.″1, 0.″2, and 0.″3 for the F200W, F405N and F410M filters respectively, are masked out by the `jwst` pipeline. The F187N observations do not have a saturated center.

2.2.1 Centering

For centering purposes, I generated a perfectly centered model PSF using `webbpsf` (Perrin et al. (2014)) – as shown in Figure 2.2 – by fitting a SED to HL Tau's photometry (e.g., Figure 2.3). The centering algorithm compares the generated PSF to the PSF in the science data in order to correctly align the image frames. HL Tau presented a particular challenge with centering due to its asymmetric stellar envelope which cannot be replicated with `webbpsf`. As can be seen in the top row of Figure 2.4 the envelope signal is as bright as the PSF at the two shorter wavelength channels, therefore appearing to alter the shape of the PSF and causing it to differ significantly from the `webbpsf`. To mitigate this, I carried out a customized centering approach to handle these data's unique centering challenges, by writing my own `PynPoint` centering module.

For each filter, I first performed a cross-correlation to find the offset of the pixels in each integration relative to their positions in integration 0: the image created from the first integration of the first dither. This calculation provided the values to shift all integration images to align with each other. I then masked the saturated inner core and part of the bright envelope in integration 0, thus accentuating the six PSF diffraction spikes as the dominant feature in the image. To improve accuracy in finding the PSF center, I applied a high-pass filter to integration 0 by convolving it with a Gaussian kernel. The kernel size was dependent on the filter used and adjusted to optimize centering performance. I then re-masked integration 0 in the same manner as above, and masked the corresponding regions in the simulated reference PSF. Finally, I performed a cross-correlation between the altered frame 0 and the masked and perfectly centered reference PSF. These offset values were combined with the previously calculated relative offsets for each image to shift all images to the center and produce the final set of aligned and centered images. The centering process is demonstrated in appendix A, and the centered products for each filter can be seen in Figure 2.4.

2.2.2 PSF Subtraction

To prepare for PSF subtraction, the outer and inner regions of the images needed to be masked to remove the saturated inner core (along with pixels heavily afflicted by associated charge migration), and outer edges of the image that appear after de-rotation. In my final reductions I kept an annulus of inner $0\farcs2$ and outer radius $2\farcs0$ for the two short wavelength filters, and $0\farcs3$-$4\farcs0$ for F405N. For F410M where the inner saturation was more severe, I constrained the inner radius to $0\farcs8$ and kept the outer radius to $4\farcs0$. I subtracted the PSF

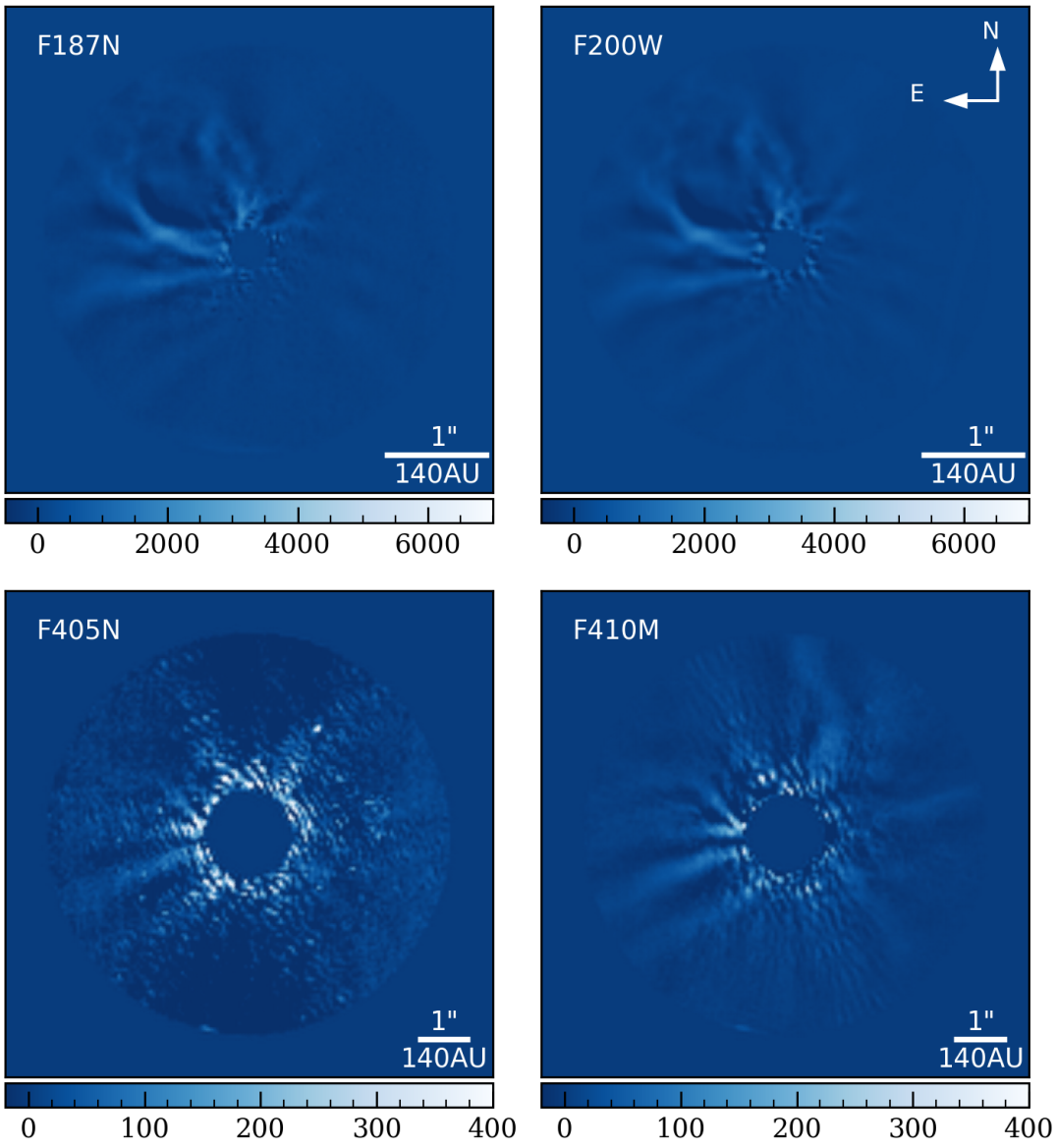

Figure 2.5: ADI PSF-subtracted data for all 4 filters where color is in units of MJy/sr. I utilize an annulus of inner radius 0.″2 for F187N and F200W. I used a larger 0.″9 and 0.″8 mask for F405N and F410M respectively, since both suffer from high levels of saturation. PSF subtraction was performed using ADI with the two angles of observation, 10° apart. The residuals show severe self subtraction from the envelope.

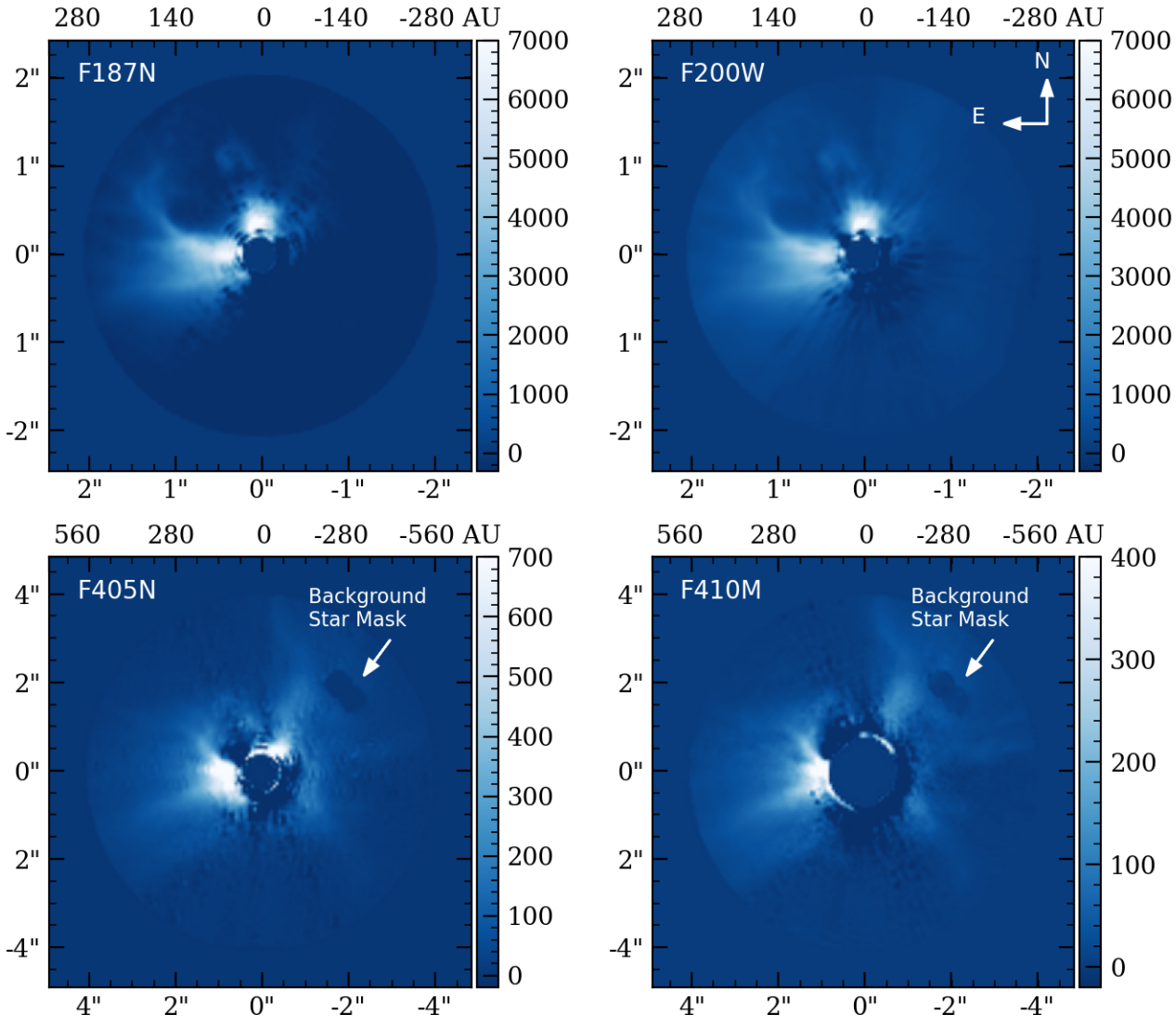

Figure 2.6: RDI PSF-subtracted data for all 4 filters where color is in units of MJy/sr. I utilize an annulus of inner radius 0.″2 for F187N and F200W, and 0.″4 for F405N. I used a larger 0.″8 mask for F410M – which suffers from high levels of saturation – to retain data in the outer envelope regions. I use RDI with MWC 758 as the reference. The stellar envelope is the most prominent feature in my data. Negative spiral residuals out to a distance of $\sim 1''$ have been introduced by using MWC 758 as a PSF reference. In addition, I applied a mask to an artifact introduced in the NW direction of the long wavelength images due to the presence of a background star in the MWC 758 data.

using a technique known as Principal Component Analysis (PCA; Amara & Quanz 2012; Soummer et al. 2012). The PCA algorithm requires a target image and a reference image. In classical ADI the reference image would be data taken at one telescope angle, and the target image from another. Orthogonal basis vectors are obtained from the reference image, with the maximum number of bases being the number of frames in the reference (n). Each of these basis vectors are multiplied with the target image, where vector 1 contains only information from the highest contrast in the reference image, to vector n containing data with the least contrast. The product images are then subtracted from the target image, creating n final image stacks. A graphic illustrating this process is available in appendix A.

The standard method used for the other targets in this GTO program was to use one telescope roll angle as the target image, and the other angle as the PCA PSF reference image, a version of classical ADI. Naturally, this technique was the first that I attempted on the HL Tau data. As can be seen in Figure 2.5, the residuals were greatly contaminated with negative side-lobes, making it apparent that roll-subtraction was an ineffective PSF subtraction technique for HL Tau. These negative regions were caused by the stellar envelope being bright and azimuthally extended at near-IR wavelengths, leading to self-subtraction between the two roll angles. In such a scenario, RDI can be a more effective PSF subtraction technique, but no reference stars were imaged during these observations to allow for an ideal star match. In light of this, I instead used another program target, MWC 758, as the PSF reference. MWC 758 was observed using the same filters, number of integrations, and subarray as with HL Tau. The MWC 758 files used as the PSF reference were `calints` files that were centered using `PynPoint`. With the use of MWC 758 as a PSF reference (as opposed to roll-subtraction), my results greatly improved; they can be seen in Figure 2.6. The PSF was subtracted from the data after the use of $\sim$8 principal components for each filter.

The disadvantage to using MWC 758 as a PSF reference, was the difference in SED shape between HL Tau and MWC 758. In addition to the two stars having different spectral types, HL Tau is partially obscured by its envelope, which modifies its SED. As a result of this and because MWC 758 possesses its own disk, the residuals suffered from over-subtraction, leading to loss of usable signals at the inner-most separation. This over-subtraction likely hinders the contrast performance (especially at $< 1''$ separation), which is discussed further in section 2.3.2. I also tested PSF subtraction with PDS 70 as a reference, but the results were inferior.

In an ideal case, I would have had a reference star with the same spectral type as HL Tau, which would be used as a PCA PSF reference without the disadvantage of the reference star

having its own disk. In lieu of a reference star I decided to test synthetic PSF subtraction, where I attempted to create the perfect PSF reference using entirely simulated data. The concepet of the algorithm was to use a library of monochromatic PSFs to construct a PCA reference image. I generated a series of monochromatic PSFs with `webbpsf` and then fitted each pixel with a Legendre polynomial to get a cube of coefficients that can be used to build any arbitrary PSF. To test the concept, I used the monochromatic PSF library as a reference for the PCA basis and subtracted it from a perfect NIRCam `webbpsf` as seen at 4μm. Theoretically, this process should give a perfect subtraction, and the results were as expected, as seen in the top row of Figure 2.7. While this method worked adequately when tested on a `webbspf`, it failed when applied to the HL Tau data due to some discrepancy between the science data and the perfect `webbspf`. This was not unexpected considering the HL Tau images are not perfectly centered, have a diffused background from the envelope, and are not point source-like in the central region; all of which could "fatten" the PSF speckles.

I performed a series of tests on the `webbpsf` to attempt to mimic these 3 factors and to see what would cause the subtraction to fail. First, I tested adding a faint halo to the PSF as a means of mimicking the envelope, where the halo is a distribution of pixels decreasing in value as 1/r (where r is the radius from the center of the image). In the residuals seen in the second row of Figure 2.7 it is clear that the presence of a halo affected the ability of the algorithm to subtract the PSF. In regions without PSF speckles the halo was retained in the final products – an ideal scenario considering the halo represents science data I'd want to preserve – however, the PSF arms were over subtracted. Next, I tested the effect of convolving the PSF with a 2d normalized Gaussian kernel to mimic the PSF spread due to HL Tau not being a perfect point source. If the PSF reference frames were left un-convolved, the PSF was not adequately subtracted, so I convolved the Legendre PSF reference images with the same 2d Gaussian kernal that was applied to the "science" `webbpsf` image. The results shown in the third row of Figure 2.7 display the desired result with the PSF being nearly completely subtracted. Finally, I tested the combined effects of convolution and a halo, while convolving the PSF references to see how re-introducing the halo would affect the abilities of PCA to subtract the PSF. Unfortunately, the PSF was still over subtracted, showing that the effect of the halo dominates over convolution. While this technique could have yielded the ideal PSF subtracted if perfected, unfortunately, due to timing constraints with the 1-year public release of my data, we decided that the time required to perfect this technique would not be worth the potential payoff of the results. The results from Figure 2.6 were deemed satisfactory by my collaborators, and so I decided to proceed with that version of the data reduction. A version of this method is currently being tested on the PDS 70 data

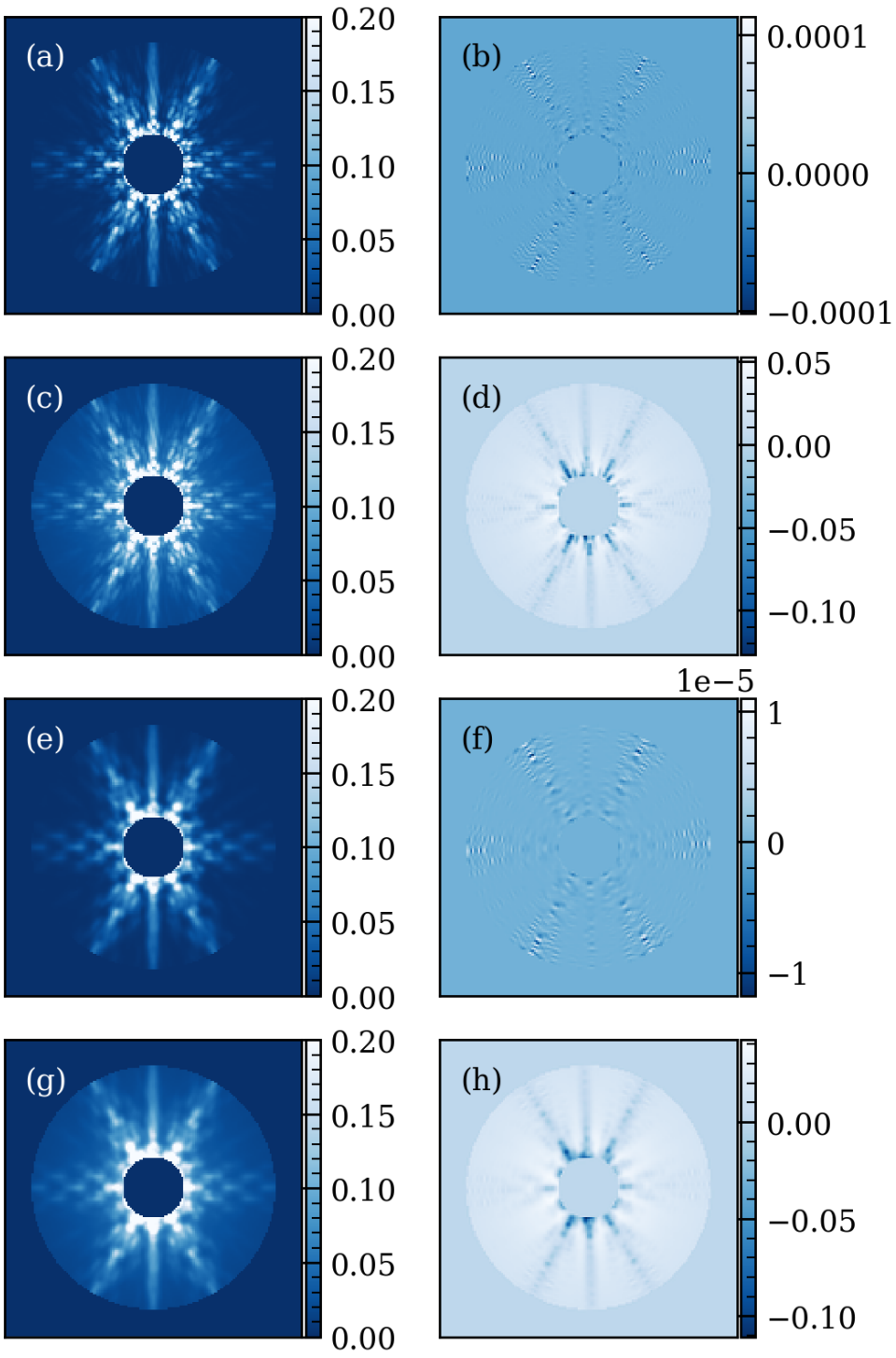

Figure 2.7: Synthetic PSF testing. (a) A standard `webbpsf` as seen through F410M. (b) The residuals of subtracting legendre polynomials created from `webbpsf`. (c) PSF with added halo. (d) The residuals of subtracting legendre polynomials. This shows over subtraction in the regions with the PSF. (e) PSF convolved with 2d Gaussian kernel. (f) The residuals of subtracting legendre polynomials. This shows near perfect subtraction. (g) PSF convolved with 2d Gaussian kernel with a halo. (h) The residuals of subtracting legendre polynomials. This shows over subtraction in the regions with the PSF.

(Leisenring et al, in prep).

2.3 Results

The results of my PSF subtraction for all filters can be seen in Figure 2.6. The disk itself is not visible in any filters due to strong saturation in the inner-most angular separation of the data and obscuring by the envelope. No planet candidates were detected in the residuals. The surrounding envelope is prominently detected in all 4 filters. The extended stellar nebula contains many features of interest, including a north facing streamer extending past 4″ and a NE c-shaped structure near the inner disk extending to around 1.″5. This structure appears to be part of a previously identified outflow cavity which will be discussed further in section 2.4.1. I also tentatively detect part of a SW spiral streamer at 4 μm (previously detected in the form of HCO^+ emission), which is discussed in section 2.4.3. In addition to the nebular features, I detected a seemingly detached "hook-shaped" feature along the north side of the outflow cavity. This feature appears at $\sim$1.″8 separation from the central star, and is distinctly detached from the cavity material in all four filters. This feature appears to have been detected before at different wavelengths, though it has never been explicitly mentioned – see Section 2.4.1 for more information.

2.3.1 Synthetic Planet Injection

Due to high saturation of the star in the data, which prevented me from taking an accurate flux measurement, I utilized the same method as with SAO 206462 (Cugno et al., 2024) to determine the point-source detection limits, where the PSF of the standard G star P330-E was used for synthetic planet injections. P300-E was observed by NIRCam (PID 1538) on 2022-08-29, using all available detectors and filters with the SUB160 subarray. The observations of this star are reported in Table 2.1. This choice of synthetic planet injection allowed me to compute accurate photometric calibration limits but prevented me from obtaining contrast with respect to the central star. To obtain calibrated flux limits, I took a scaling factor applied to P330-E's PSF and combined with the flux of the standard star ($f_\star$ in equation 2.3); 20.17 mJy, 21.23 mJy, 5.81 mJy and 5.84 mJy for F187N, F200W, F405N and F410M, respectively (Rieke et al., submitted to AJ).

Due to the presence of the envelope, sensitivity estimates for these data varied by angular separation from the star and position angle around the star. The regions dominated by envelope flux could not be used to calculate 5σ sensitivity, since the envelope dominates over background noise, preventing an accurate noise calculation. Therefore, when calculating

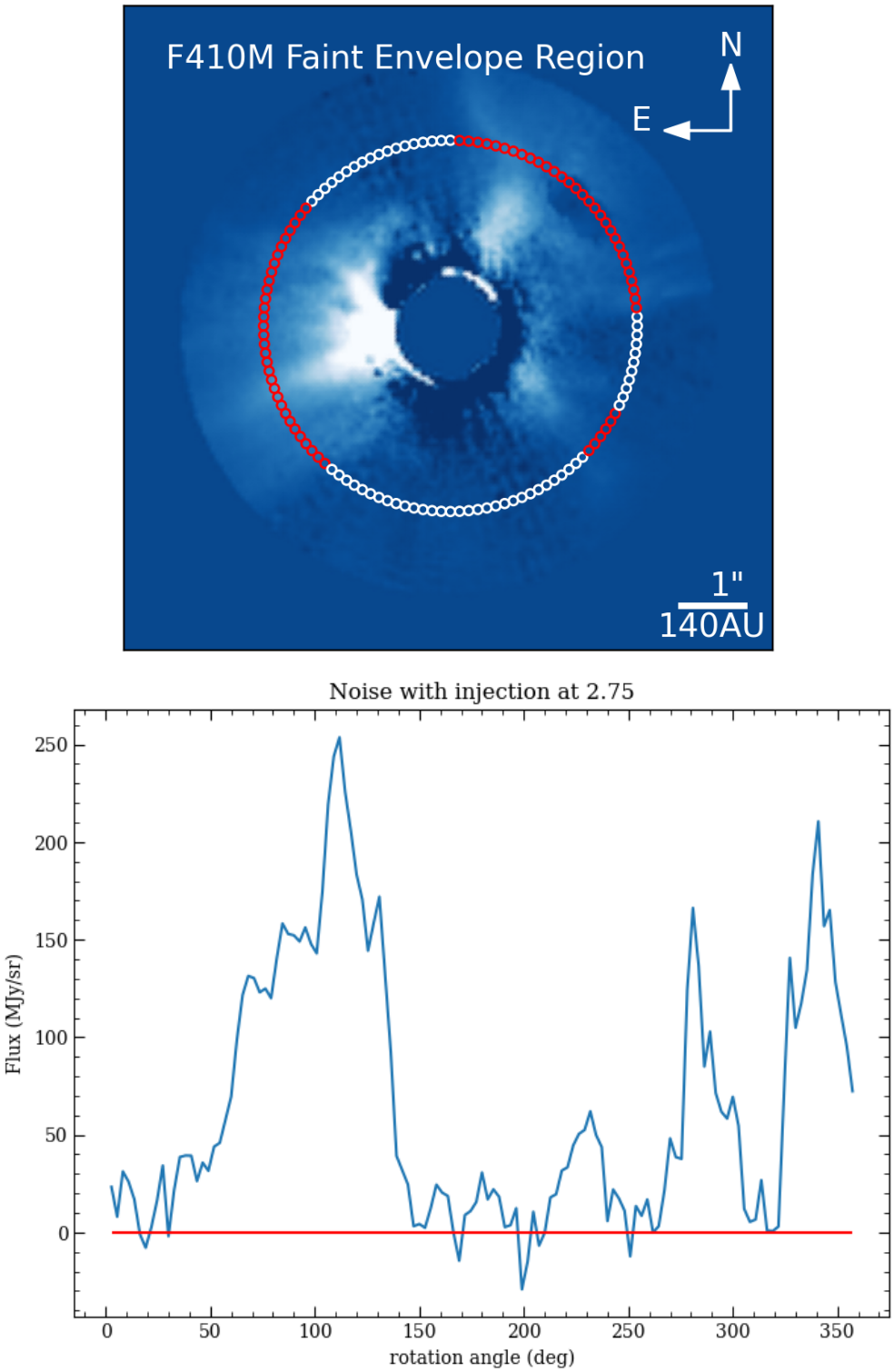

Figure 2.8: Noise profile for aperture injection at 2.″75 separation. The red apertures correspond to the > 2FWHM spikes in the noise profile shown in the bottom panel. These regions are considered to be contaminated by envelope signal. The white apertures correspond to the rest of the profile centered around the red 0 line on the bottom panel. These regions are accepted as valid noise measurements.

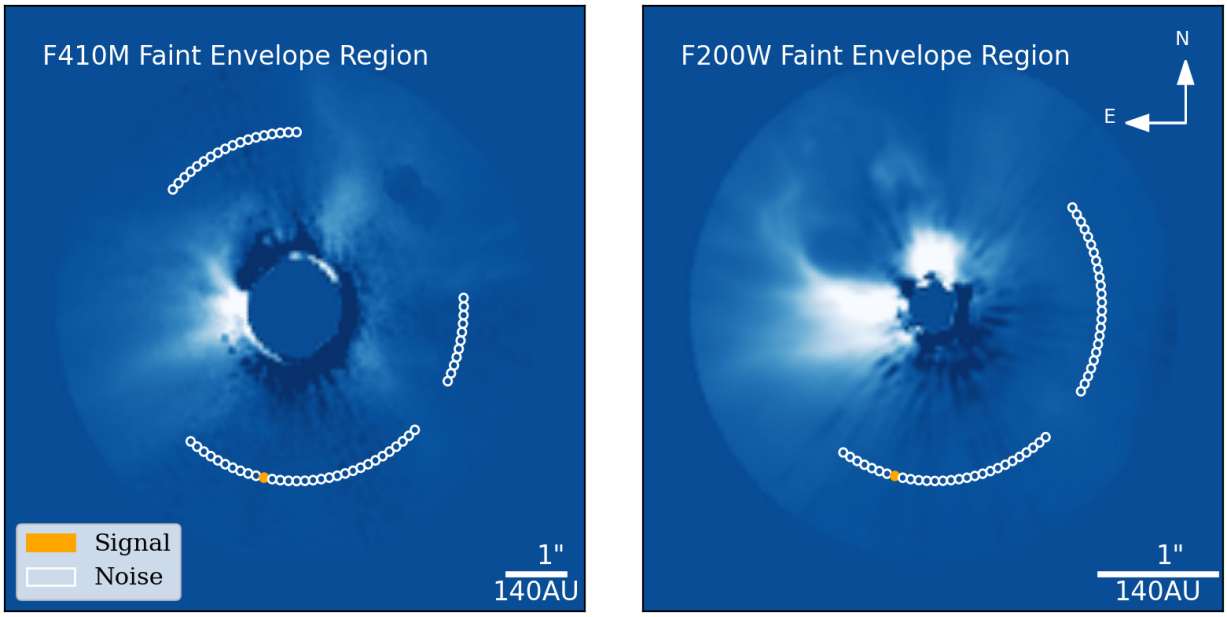

Figure 2.9: Example of how I injected signal and noise 1 PSF FWHM diameter circular apertures, depending on the position angle of the injected planet, and the filter used. A companion injected in an area of low envelope flux will only utilize apertures in low flux regions as a means of accurately measuring the noise. These valid regions are determined in the manner illustrated in Figure 2.8. The regions that are determined to have low envelope flux differ greatly for each wavelength and angular separation.

5σ sensitivity I only considered areas where the envelope readings flatten out and fluctuate around zero (comparable to background noise). I determined high and low envelope flux areas by computing an azimuthal noise profile for each angular separation from the central star. An example of this is shown in the bottom panel of Figure 2.8. To determine the baseline noise value in a low envelope flux region, I took an area in my reductions with low envelope flux (selected by analyzing the noise profile) and computed the standard deviation of the independent noise apertures in that area. In Figure 2.8, this could correspond to the apertures between 150 and 210 degrees. I then defined all apertures with a noise value greater than 2σ from the base-line noise to be in an area of high envelope flux and exclude those from my signal to noise measurements. These excluded areas are displayed in red in the top panel of Figure 2.8. Note that the masked-out background star in the NW part of the $4\mu m$ data is also treated as envelope, despite reading as 0 flux.

2.3.2 Sensitivity Limits

I measured sensitivity by placing a circular aperture with diameter equal to 1 FWHM of the P330E PSF at the position of the P330E injection. I took the sum of pixel values in the aperture to give a flux measured in Jy. In order to account for noise present within the signal aperture which could artificially elevate the signal, the values within the noise apertures were subtracted using the following equation. Let F equal the value within the flux aperture, and $\overline{N_{\text{arr}}}$ equal the mean of the values within the other apertures, then signal S is given by equation 2.1.

$$S = F - \overline{N_{\text{arr}}} \tag{2.1}$$

At the same angular separation from the star, I placed apertures in positions of negligible envelope flux and took the standard deviation of the values in those apertures to estimate the noise N.

$$N = \sigma_{N_{\text{arr}}} \times \sqrt{(1 + \frac{1}{len(N_{\text{arr}})})} \tag{2.2}$$

The term multiplied by standard deviation $\sigma_{N_{\text{arr}}}$ in equation 2.2 accounts for small sample statistics when a limited number of apertures are used. An example showcasing the signal and noise apertures can be seen in Figure 2.9. Different scaling factors were applied to the injected P330E synthetic planet until $\sim 5\sigma$ (defined here as $S/N = 5$) was reached. The scaling factor is defined as the magnitude of the planet with respect to the central star. This apparent magnitude mag was converted to planet flux f_p using equation 2.3.

$$f_p = 10^{mag/2.5} \times f_\star \tag{2.3}$$

Artificial planets were never injected in regions with high envelope flux. As a result, most of the points on the contrast curves only correspond to the SW and W regions of the data. In the inner $< 1\farcs5$ separation regions where severe over subtraction and negative MWC 758 spirals are present, all measurements were taken conservatively since the noise is this region could have been artificially low.

The sensitivity limits and corresponding mass limits in the low envelope flux regions can be seen in Figure 2.10. I note that due to both envelope obscuring and high saturation, NIRCam cannot detect the theorized Saturn mass planets at ≤ 70 au ($0.5''$) separation with 5σ confidence. At the edge of the 2 μm field of view (FOV; $1\farcs8$ separation), the deepest limits are in the F187N filer, reaching $\sim$40 μJy. At the edge of the 4 μm FOV ($3\farcs75$) F410M reaches the deepest limits of $\sim$10 μJy. Regarding the areas with high envelope signal, I inspected

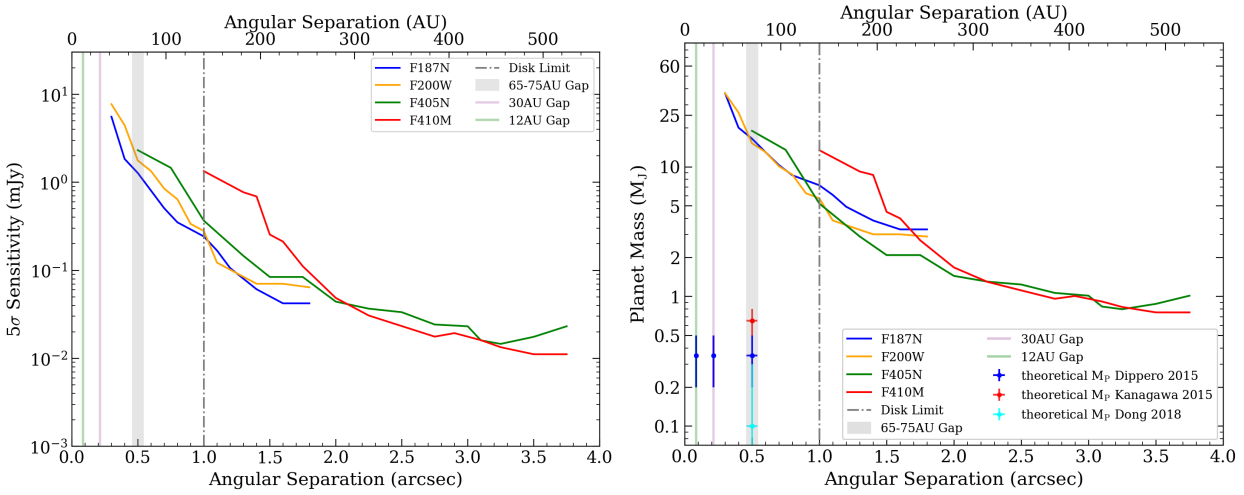

(a) Sensitivity (b) Mass

Figure 2.10: (a) NIRCam 5σ sensitivity limits for HL Tau as a function of separation from the central star. These values are only for regions with faint or no envelope detection. The edge of disk – $\sim$1$''$ as imaged by ALMA Partnership et al. (2015) – is represented by the vertical dash-dot grey line. The major disk gaps possibly hosting planets are plotted as vertical shaded regions. Due to saturation, only the 65-75 au gap is within my unmasked region. (b) Mass limits using BEX evolutionary track models when $M_{\rm p} < 2M_{\rm J}$ and AMES COND models for larger masses. In the low envelope flux areas I reached limits as deep as $5.2M_{\rm J}$ at the disk edge in the F405N filter (assuming planets are 1Myr old). My deepest limits are $\sim 0.75M_{\rm J}$ out to 4$''$. Points showing the approximate masses of the theoretically predicted planets are plotted in the major disk gaps to provide context.

the data visually to look for planet signatures since I cannot quantitatively calculate 5σ sensitivity without an accurate noise measurement in those areas. No clear point sources were found in those regions.

To estimate detection limits in planet mass units, I used BEX (Linder et al., 2019) evolutionary tracks for planets with mass $M_{\rm p} < 2M_{\rm J}$ and AMES-COND models (Chabrier et al., 2000) for more massive companions. To calculate mass, I converted f_p to the flux corresponding to absolute magnitude (f_{10}) using equation 2.4. A full derivation can be found in appendix B. These logged f_{10} then correspond to a planet mass in the isochrones.

$$log(f_{10}) = log(f_p \times (\frac{d}{10})^2) \tag{2.4}$$

Since no isochrones were available for planets as young as 0.1 Myr (estimated age of HL Tau), I chose the youngest available age of 1 Myr when interpolating companion masses. In such evolutionary tracks, the older the planet, the more massive a planet with the same

brightness must be to be detected, since older planets emit less in the IR. Because the system is younger than 1 Myr, and could have even younger planets, my mass estimates may be conservative since the limiting mass would decrease if the planets are younger. It should also be noted that these evolutionary models are less well constrained at young ages, and therefore the results for young systems are less robust. The results in sensitivity flux units should be taken as more physically meaningful than in mass units.

In order to obtain mass limits in the disk regions of my data where planets are commonly searched for (0.″2-0.″8), I used a 0.″2 radius inner mask for the F187N, F200W and F405N filters. At these separations, the data are sensitive to companions with $M_{\rm p} > 8.6\ M_{\rm J}$. At angular separations out to 1″ (the outermost edges of the disk), the data are sensitive to $M_{\rm p} \gtrsim 7\ M_{\rm J}$ for F187N, $M_{\rm p} \gtrsim 5.7\ M_{\rm J}$ for F200W, and $M_{\rm p} \gtrsim 5.2\ M_{\rm J}$ for F405N. For F410M, which suffers from the most over subtraction at inner angles, the 1″ limit is $M_{\rm p} \gtrsim 13\ M_{\rm J}$. We are most sensitive in regions outside the disk past 2″ (∼260 au) where any remaining envelope obscuring is greatly reduced. At 2″, in the low envelope flux regions, the data reach ∼3 $M_{\rm J}$ for the short wavelength filters and ∼1.5 $M_{\rm J}$ for long wavelength ones. The deepest limits are ∼0.75 $M_{\rm J}$ at 3.″75 (525 au) separation in the F410M filter.

2.4 Discussion

2.4.1 Outflow Cavity

Past envelope imaging done by Stapelfeldt et al. (1995) with HST and Close et al. (1997) with CFHT, revealed a c-shaped cavity produced by a jet extending NE 1″ in length, centered 1.″2 from the central star. These observations have since been replicated with deeper imaging done by various telescopes. In turn, I resolve similar structures with NIRCam, and compare to 2004 HST observations from GO program 9862 as shown in the middle row of Figure 2.11. The c-shaped outflow cavity seen with HST appears narrower at 0.6 μm than with NIRCam; most clearly evident in panel (e) of Figure 2.11. While the cavity opens at approximately the same rotation angle, the structure which curls tightly inwards at 0.6 μm, opens more widely at 2 μm and 4 μm and extends outwards past 4″. This broadening of the c-shaped cavity at longer wavelengths is consistent with the Close et al. (1997) observations, and likely due to the change in optical depth with increased wavelength. This is clearly demonstrated in Figure 1.3, where the color progression from blue to red which traced different parts of the envelope, follows an increase in wavelength. The faint structure in panel (d) extending vertically north aligns with a previously identified streamer seen clearly at 4 μm and faintly at 2 μm. As evident by the HST contours, this feature shifts west at longer wavelengths,

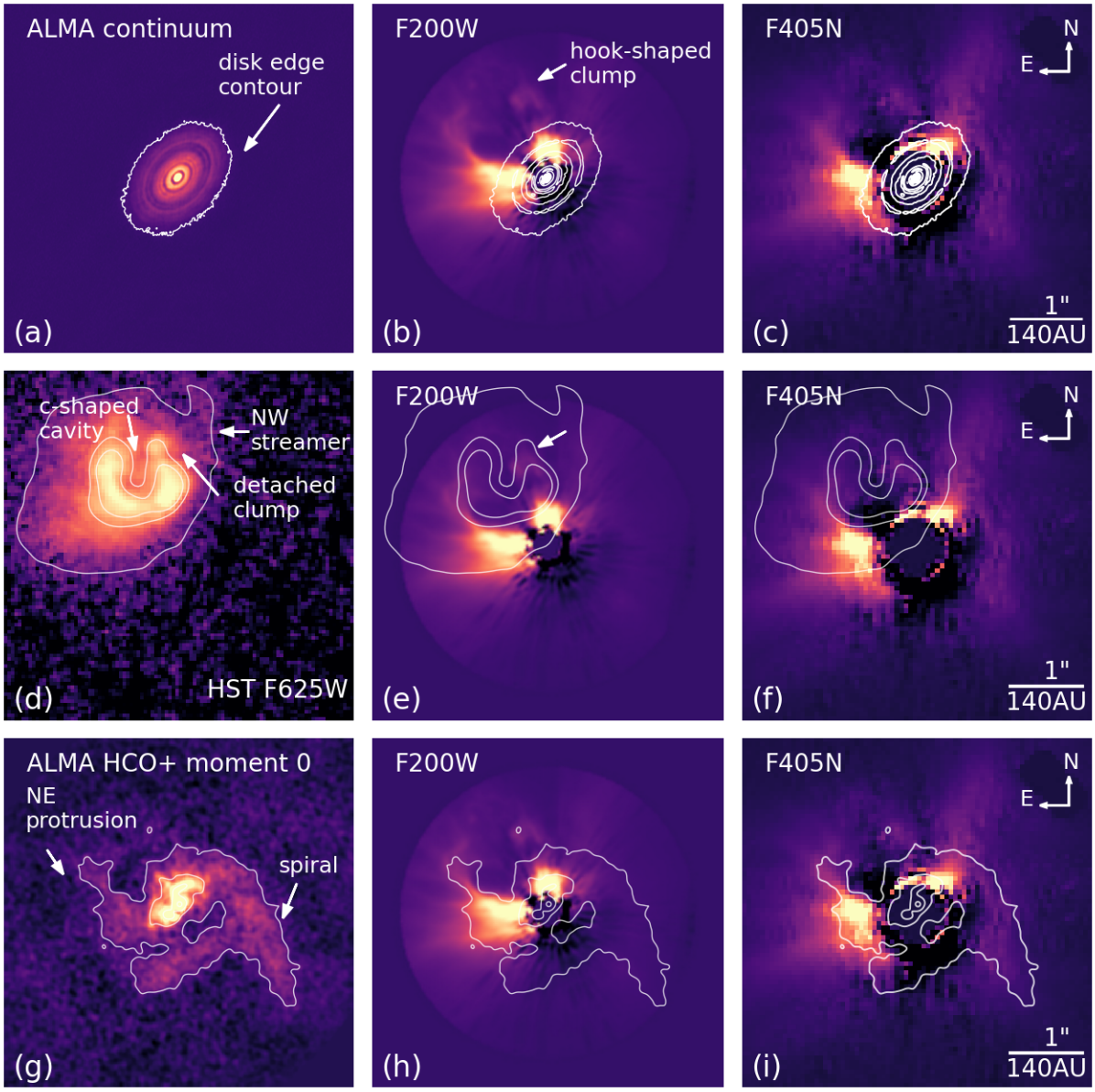

Figure 2.11: Comparing features in my data with observations taken at different wavelengths. In all panels the star is located at the center, and the stellar position from the other datasets were manually aligned. ***Top***: (a) ALMA Partnership et al. (2015) mm continuum emission. (b) F200W residuals overlaid with ALMA contours to showcase the disk and gap locations. The disk is not visible to NIRCam. A notable hook-shaped clump is visible in my data a the edge of the outflow cavity. (c) F405N residuals overlaid with ALMA contours. ***Middle***: (d) 0.6μm HST data from PID9862 (log scaled). (e) Comparison to F200W. The c-shaped outflow cavity is broader at 2μm. The white arrow points to the same hook-shaped clump seen in panel b. (f) Comparison to F405N. The cavity is broader, and the upward stream is shifted west. ***Bottom***: (g) ALMA HCO^+ moment 0 map from Yen et al. (2019). (h) Comparison to F200W. The spiral is not clearly detected at this wavelength, but the NE protrusion clearly aligns. (i) Comparison to F405N. I detected a structure which appears to coincide with the HCO+ spiral.

which is also consistent with Close et al. (1997), where there is a clear separation between the red and blue parts of the streamer.

The hook-shaped clump mentioned in section 2.3 is potentially detected in the HST and LBTI data (see Fig 1.6) which also shows a detached feature on the northern side of the c-shaped cavity. If this is the same feature, then it is further separated in the HST data ($\sim$1.33″). Whether this is due to different wavelengths, or a sign of radial shift over time is uncertain. However, when comparing the 2004 HST data at 0.6 μm shown here with the results from Close et al. (1997) at 0.9 μm and 1.6 μm the clump consistently "moves" inwards with increasing wavelength. Therefore it appears the clump position is wavelength dependant. Material I associate with the clump is also faintly visible in the Yen et al. (2019) data, and is possibly at the same location as with JWST/NIRCam, as shown by the small contour overlapping the clump in panels (h) and (i).

2.4.2 Comparison to Past IR Observations

Overall, these NIRCam observations provide an impressive picture of HL Tau in the IR. Previous imaging with Subaru in the near IR by Murakawa et al. (2008) revealed the extended structure of the envelope in J (1.25 μm), H (1.63 μm) and K (2.2 μm) bands, shown in Figure 1.4. These observing wavelengths would be most comparable to my F187N and F200W NIRCam observations. The total intensity images in the top row of Figure 1.4 revealed the extent of the stellar envelope and the prominent northern extended structure, which is faint in our $2\mu m$ data. The polarized intensity images on the bottom row are more visually comparable to our data, though the nature of the observations do not allow for the same level of fine structure seen with NIRCam. The NIRCam observations in F405N and F410M showcase a similar extended envelope structure to Murakawa et al. (2008) – such as an extended feature to the north ranging past 4″ – but at different wavelengths to the Subaru observations. The SW structure visible in the Subaru polarized data, does not appear to align with any of our total intensity NIRCam observations. This hook shaped clump also appears visible in the Murakawa et al. (2008) observations, as indicated in Figure 1.4, though it was not highlighted in the 2008 observations.

The Testi et al. (2015) infrared observations recovered some envelope structure in K band – mainly the outflow around a position angle of 90° – and minimal signals around 300°. They detected the same signals in L band, but less prominently in the residuals overall, as is shown in Figure 1.6. My reductions reveal the same basic envelope structure in these areas with the addition of more fine structures and details. It should be noted that the lack of envelope

structure in the Testi et al. (2015) observations is likely due to the data reduction technique they used which subdues the envelope signal. A similar technique could have been used on this data, but it was decided that the envelope signal was valuable to keep.

2.4.3 Streamers

In the bottom row of Figure 2.11, I compare my observations to the Moment 0 map from Yen et al. (2019). As mentioned in section 1.5, Yen et al. (2019) detected a SW extending spiral arm of infalling envelope in HCO^+. The spiral has a length of 3″ starting from the north, then bending around the star, and extending to the SW. The same spiral appears to be visible in this data, as well as a NE extending feature tracing the c-shaped outflow cavity. I detected a portion of the spiral arm wrapping around the disk in F405N, and extending out to 3″ at 4 μm. The position of the NIRCam spiral aligns with the HCO^+ spiral, though the shape is somewhat different at IR wavelengths. The feature I detect traces a different component of the spiral than HCO^+ gas: IR light scattering off dust tracing the spiral shape.

Infalling streamers are likely continuously fed from the surrounding envelope, allowing the structures such as this one to survive for an extended period of time. Over the disk lifetime, a large streamer such as this with a mass infall rate of $\gtrsim 5\ M_{\rm J}\,{\rm Myr}^{-1}$ could greatly increase the mass available for planet formation (Gupta et al., 2024). If planet formation is ongoing in the disk, then this streamer is providing an influx of new material to the system for the planet(s) to accrete. The spiral streamer is not clearly detected in either of the short wavelength filters. Its absence can be seen in panel (e) of Figure 2.11. I do detect very faint structure at 2 μm which traces the shape of the spiral seen at 4 μm, but the inner part is not clearly visible. The dust and gas tracing the spiral streamer appear to have a composition such that they only peak at wavelengths > 2 μm. The NW streamer also has a more robust detection at > 2 μm, though it is more clearly visible at 2 μm than the SW spiral, suggesting it may be composed of different material than the SW spiral.

2.4.4 Constraints on Planet Detection

The sensitivity limits are hindered by high saturation at inner angles. It should also be noted that the saturation levels were not due to instrument error, but 10-20% higher throughput than was initially anticipated. As expected, I was unable to reach the depth needed to detect the theoretically predicted planets within the disk region – sub-$M_{\rm J}$ at $\leq 1''$ from the star. The limiting factor is mainly the presence of the envelope. Young-hot planets peak in the near-IR (shorter wavelengths) and become fainter at longer wavelengths; however, HL

Tau's envelope becomes more opaque at shorter wavelengths. It should be noted that while extinction from the envelope would factor into my ability to detect companions, I assumed all companions injected were foreground objects (not subject to extinction). Given this, the estimates listed here are the most optimistic case in terms of extinction. In reality, any possible planets should experience envelope obscuring.

When comparing to IR imaging in the L′ band done by Cugno et al. (2023) and Testi et al. (2015), my limits are comparable in the 4 μm filters if I use the same evolutionary tracks to calculate planet mass. Both studies used similar data reduction methods to me; a combination of ADI and PCA. I took sensitivity measurements both in the same inner region and further out than Testi et al. (2015) and Cugno et al. (2023) to a separation of 525 au. While companions at this distance were not the primary target, it is still possible that a planet could exist outside the disk region as seen in recent papers by Cugno et al. (2024) and Pearson & McCaughrean (2023) where planet candidates were detected at wide separations from their stars. The Cugno et al. (2023) NaCo-IPSY survey (3.8 μm) reached $\sim$9 $M_{\rm J}$ at 1″ and $\sim$5 $M_{\rm J}$ at 2″ using the same evolutionary tracks as me. Comparing to my low-envelope region observations in F405N, I reached $\sim$5.2 $M_{\rm J}$ at 1″ and $\sim$1.4 $M_{\rm J}$ at 2″. Therefore, my observations reached a few $M_{\rm J}$ deeper than VLT/NaCo, as would be expected. The Testi et al. (2015) LBTI/LMIRCam observations achieved an absolute magnitude of $\sim$11.2 at 1″ – corresponding to a mass limit of $\sim$3.8 $M_{\rm J}$ using the evolutionary tracks adopted in this work – which is deeper than my observations. These deeper limits likely result from Testi et al. (2015) suppressing the envelope signal, allowing for a lower background limit, as is displayed by the reduction in envelope signal in the right panel of Figure 1.6. To subtract the envelope, they assume that no point sources would be detectable in K band (2.2 μm) and use the K band results to subtract the envelope from their L′ data. If a similar method were applied to my data, then I would perhaps reach deeper limits than are achieved here. Future work focused primarily on deep detection in embedded disks could explore this further.

Comparing my limits to other PID1179 targets, MWC 758, SAO 206462 and HL Tau all manage to achieve a depth of $\sim$1-10 μJy at 4″. The depth reached in each filter relative to the others differed for each object. For MWC 758, the F405N filter consistently reached deeper than F410M. For my data and SAO 206462, F405N reaches deeper at separations $\lesssim$ 1-1.5″, while F410M generally surpasses F405N at larger separations. This is likely due to saturation at the inner angles where the brighter-fatter effect and charge migration hinder sensitivity in F410M. At $<$ 2″ separation MWC 758 and SAO 206462 reach the deepest limits in F187N, while for HL Tau F187N generally reaches deepest in sensitivity but not in mass limit. These results for HL Tau were not as deep as had been hoped for the

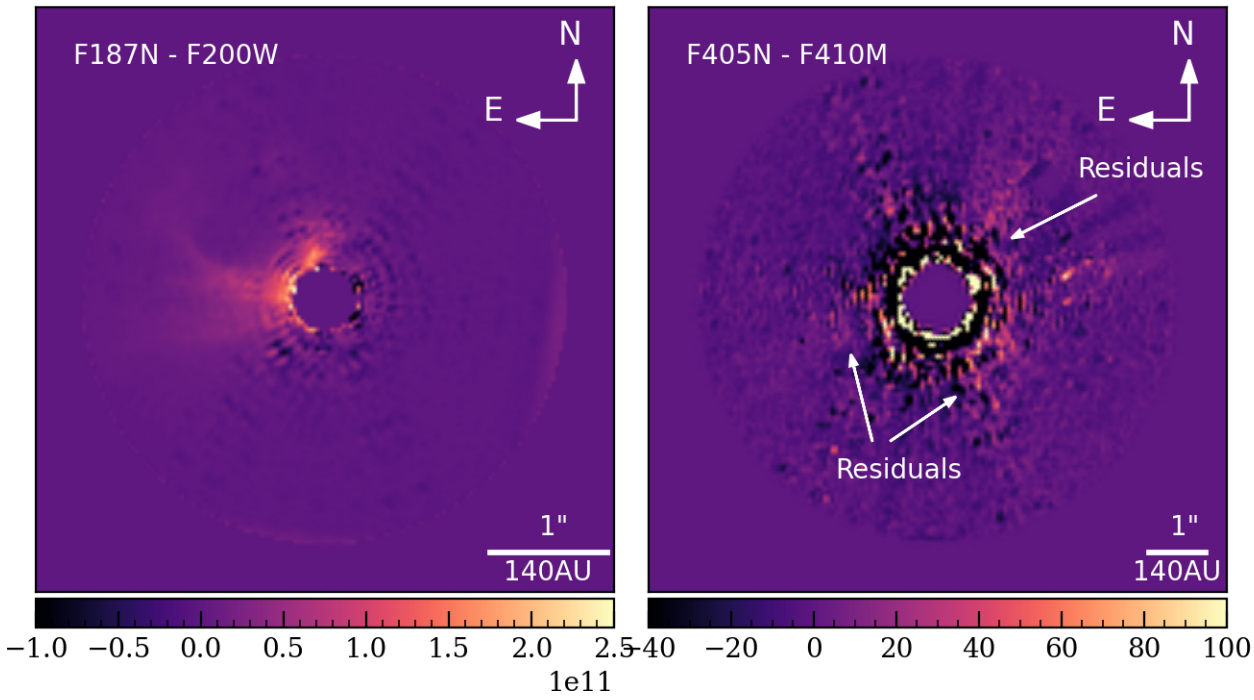

Figure 2.12: Continuum subtracted residuals for F187N (Pa-α) and F405N (Br-α). The faint residuals shown in the left panel could indicate Pa-α accretion shocks in the disk region, though they could be a result of an incomplete subtraction. There are also potential signs of Br-α accretion in the disk, though it is faint.

program. The goal had been to reach the deepest detection limits for this target, but this was not possible while maintaining envelope structure. If this work were to be expanded on further, then going through a process to subtract the envelope in order to achieve deeper detection limits could be valuable. This process could look similar to the methods of Testi et al. (2015) by computing F410M-F200W and F405N-F187N (where F200W and F187N would be appropriately scaled) to subtract the envelope from the 4μm data. This should theoretically provide deeper limits, though it is possible this method of envelope suppression would also unintentionally remove any potential planet signal buried within the envelope.

2.4.5 Accretion

When comparing to past observations, I chose F405N to represent 4 μm for Figure 2.11 since the saturation of F410M obscures important features at $\leq 1''$ separation. While the morphological differences I see in F405N – as compared to ALMA and HST – can be attributed to difference in wavelength, it should also be noted that F405N is centered around the Br-α line,

and so other physics may be involved when comparing to that filter. To test for evidence of accretion I removed any continuum from F405N by subtracting the F410M data. As can be

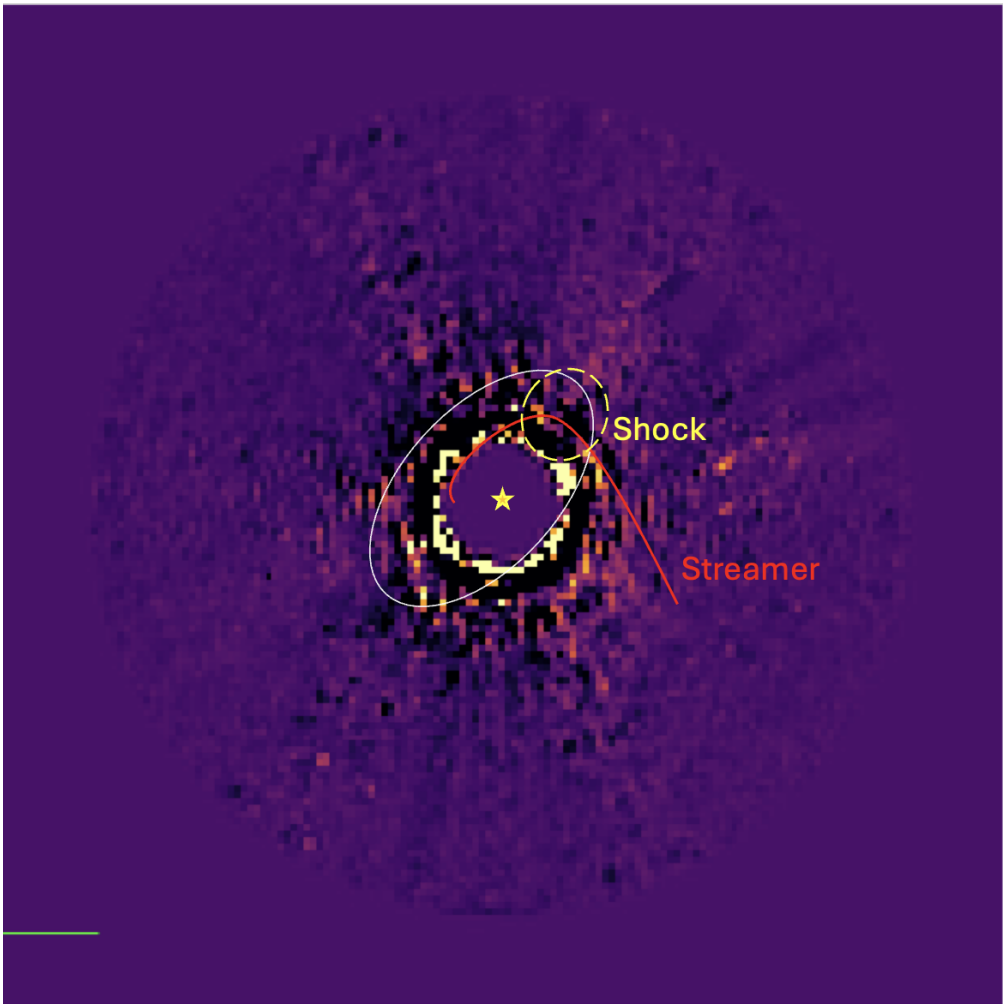

Figure 2.13: Overlay of shock region in Figure 1.5 with the right panel of Figure 2.12. The shock regions seems to align with some positive signal in the F405N-F410M residuals. The green bar in the bottom left is the 1″ scale bar.

seen in the right panel of Figure 2.12, there are tentative signs of accretion close in the disk region, as evident by the positive features in the residuals around the intersection between the disk and the NW and SW streamers. I performed a similar test with F187N, though I scaled each filter by the sum of the flux in the other (in the outer region less affected by PSF subtraction effects), since F200W is likely not an ideal representative of F187N continuum due to the difference in wavelength. It is possible the residuals seen in the left panel of Figure 2.12 indicate Pa-α accretion shocks near the disk, though the signals may also be artificial due to the scaling factor. Accretion in this filter would likely be centered around

the location of the outflow cavity, which does align with what is seen here. Garufi et al. (2022) previously detected signs of accretion shocks with SO and SO_2 in the NW disk region as highlighted in Figure 2.13; my residuals in the NW of F405N appear to align with this as shown by the positive signal appearing within the shock region.

2.4.6 Requirements to Detect Small Embedded Planets

In observational astronomy, a non-detection opens up two possibilities: 1) the instrument wasn't sensitive enough to see the object, 2) the object isn't there. Case 1 provides crucial information for instrumentalists and observers, and case 2 is passed onto theorists to find explanations as to why a predicted object doesn't exist. While case 2 is more interesting, it cannot be confirmed until case 1 is ruled out. Considering our sensitivity limits for HL Tau, case 2 cannot be ruled out (except for large planets), and case 1 appears true in terms of hitting the theoretical 0.5-0.8 M_J planet mass.

Observing smaller planets within the disk region, which is highly obscured by the envelope, does not seem to be possible at NIRCam wavelengths. Observations performed at longer mid IR wavelengths may better bridge the gap between the NIRCam envelope observations and the ALMA disk observations. Longer mid-IR observations may better penetrate the envelope, while not losing emission from young-hot planets. However, JWST/MIRI does not have the necessary angular resolution at $\leq$ 70 au to detect the theoretical 0.5-0.8 $M_{\rm J}$ gap opening planets. This type of observation is complicated with space-based instruments, since it requires both long wavelengths and high angular resolution. No current instruments have the resolution and wavelength range required for such an observation. However, probing planets in an embedded disk may be possible with future ground-based observations using a new class of Extremely Large Telescopes (ELTs). The Mid-infrared ELT Imager and Spectrograph (METIS, Brandl et al., 2021) instrument on the upcoming European Extremely Large Telescope (ELT) has planet formation and circumstellar disks as one of its primary science goals. ELT will be a complementary telescope to JWST, since both operate at a similar wavelength range and have different strengths. While JWST can detect fainter objects at a larger separation, ELT/METIS can provide higher angular resolution and sharper images (Brandl et al., 2012, 2021). HL Tau will be outside ELT's observing range, but an ELT observation of a disk like HL Tau using METIS could nicely complement a JWST/NIRCam observation with the possibility of detecting gap-opening planets.

Another upcoming extremely large telescope is the Thirty Meter Telescope (TMT). TMT will also operate in the mid-IR and will have superior resolution to JWST. Simulations have

shown that TMT should be able to detect $\leq 0.1\ M_{\rm J}$ planets at ≤ 10 au at a distance of 140 pc (Skidmore et al., 2015). This resolution would be ideal for imaging the 12 au, 30 au, and 70 au gaps in HL Tau. It should be noted that these limits (as with ELT) do not factor in the presence of an envelope, however at mid-IR wavelengths obscuring from the envelope would be less severe than as seen with NIRCam. As learned from my observations, future observations of this target or ones like it must factor in envelope flux in order to select the right instrument and observing modes when searching for planets in embedded disks. As instrumentation, observation and data reduction techniques continue to improve, case 1 will eventually be ruled out.

Chapter 3

Future Work and Conclusions

3.1 Conclusions

I made JWST NIRCam observations of HL Tau; a class I star with a multi ring and gap disk. I obtained images out to 4″(560 au), with 4 NIRCam filters, and provided a more complete picture of the dust and gas surrounding this young star, as illustrated in Figure 3.1. My main findings are as follows:

- With NIRCam's sensitivity I was able to obtain the most detailed envelope structure for this system in the IR. I detected HL Tau's protostellar envelope in all 4 filters as well as the c-shaped outflow cavity and NW streamer previously detected by e.g. Stapelfeldt et al. (1995) Close et al. (1997), Murakawa et al. (2008), and a detached hook-shaped clump on the north end of the outflow cavity (Figures 1.3, 1.4, 2.6, 2.11).

- I detected part of an infalling streamer previously detected in the form of HCO^+ emission with ALMA (Yen et al., 2019) in the 4 μm filters (Figure 2.6, 2.11). The spiral streamer is most clearly detected in the F405N filter, which is centered on the Br-α line, however the spiral feature appears to be mainly scattered light from the continuum (Figure 2.13).

- I do not detect the ALMA dust emission protoplanetary disk due to the envelope flux dominating over any disk light at 2-4 μm wavelengths. I also do not detect any protoplanet candidates.

- The deepest detection limits within the ALMA disk region are 5.2 M_J in the F405N filter – deeper than VLT/NaCo. At the edge of the FOV (4″) I reach ∼0.75 M_J (Figure 2.10).

- I see tentative evidence for Br-α accretion signatures where the disk intersects with streamers. I also see potential signs of Pa-α accretion at the intersection between the disk and the outflow cavity (Figure 2.12, 2.13).

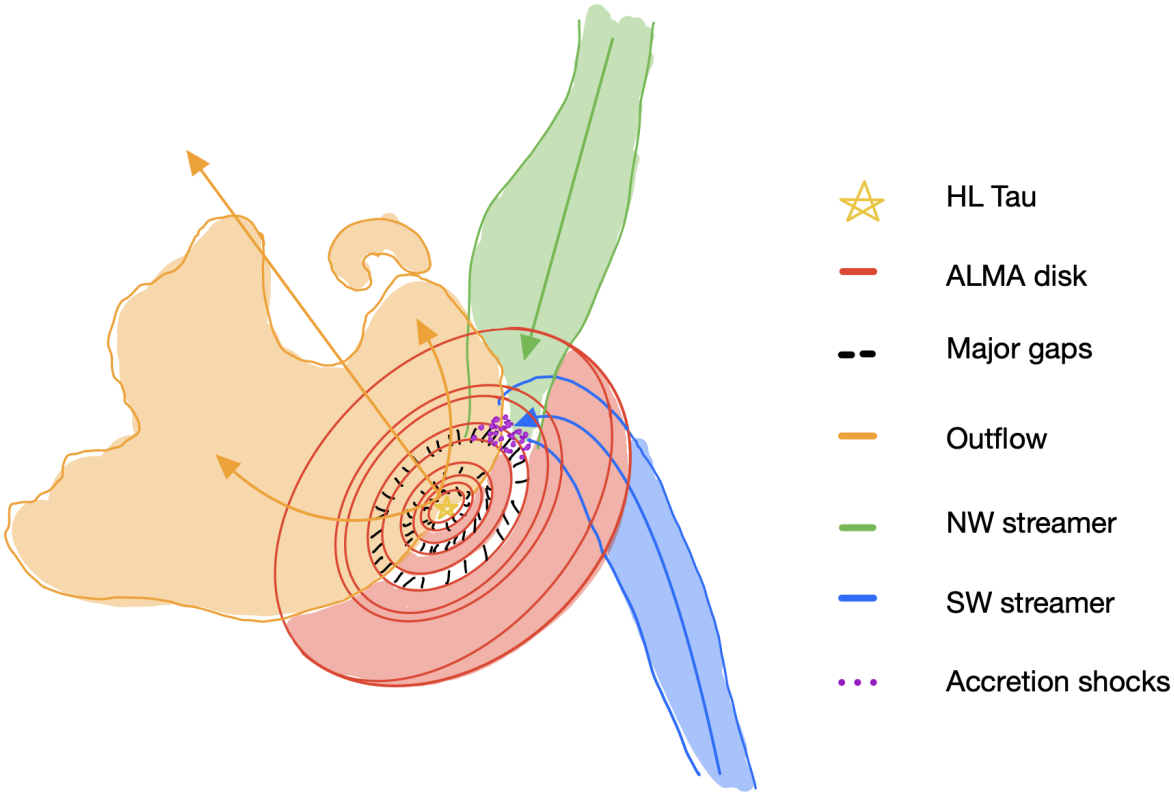

Figure 3.1: Hand-drawn diagram displaying the different major components of this system.

This work, along with Wagner et al. (2024), and Cugno et al. (2024), provide the first observations of young stellar objects with JWST/NIRCam. HL Tau is the youngest disk imaged by this instrument, providing images of its young stellar environment in unprecedented detail. Though planets in the HL Tau disk remained ever illusive, these observations helped solidify the limits of our current IR observing capabilities. It is important to push the limits of observation, and to continue studying crucial targets like HL Tau with each new instrument and observing method that is made. Through observations at different wavelengths and with increasing sensitivity, the pieces of the HL Tau puzzle are slowly being assembled. Only time will tell if this disk harbours the next earth.

3.2 Future Work

Though my work with HL Tau is complete for this dataset, there is still NIRCam GTO data that I will be involved with during my PhD. Aside from co-authoring the PDS 70 and TW Hya publications, I will be receiving GTO data for the disk HD 97048 within the next year. HD 97048 is a $\sim$ 3Myr intermediate-mass star. The goal with the dataset will be to try to directly image a companion that could be inducing a kink in the ALMA-observed velocity profile, as shown in Figure 3.2. Velocity kinks can be used as a signpost for the presence of planets in disks, since these features are easily linked to the presence of a perturber causing the kink (Bollati et al., 2021; Speedie & Dong, 2022). Pinte et al. (2019) predict a 1-5 $M_{\rm J}$

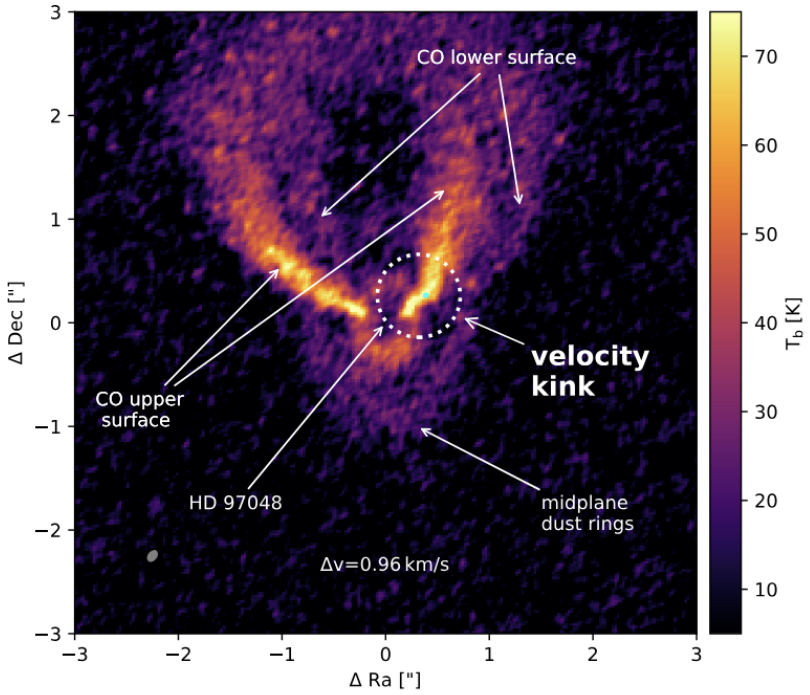

Figure 3.2: Pannel from Figure 1 of Pinte et al. (2019) showing a velocity kink in HD 97048. The cyan dot inside the white dotted circle represents the position of the perturber causing the kink. I will search for this perturber using JWST/NIRCam.

planet at 130AU ($\sim 0\farcs5$) separation could be responsible for the velocity kink. This suspected size and separation of planet should be detectable with NIRCam coronagraphy. As such, the observations will be coronagraphic using two roll angles and a reference star observation. The observations are nominally part of Cycle 2, but are scheduled for April-June 2025.

The disk has multiple rings and gaps, as shown in Figure 3.3. These features should

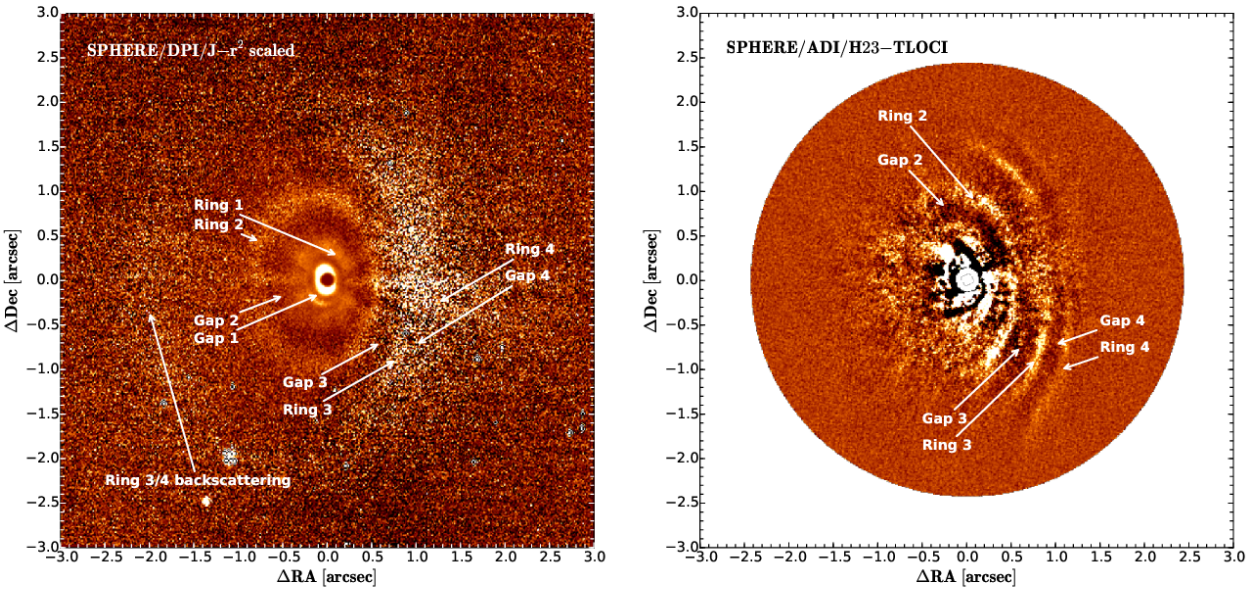

(a) (b)

Figure 3.3: Figure 2 from Ginski et al. (2016) showing (a) SPHERE dual polarized-imaging (DPI), and (b) ADI imaging of disk HD 97048. Comparable results should be attainable with JWST/NIRCam.

be visible at NIRCam wavelengths. This work will expand on the skills and knowledge I have gained from working on the NIRCam HL Tau observations. Since I will be operating at similar wavelengths, with the same instrument, several of the data reduction techniques should carry over from the HL Tau project to the HD 97048 data. I suspect I will be able to use my customized `PynPoint` data reduction pipeline, which I am now quite familiar with. Having a reference star observed could greatly improve PSF subtraction in the event that ADI does not allow for adequate contrast to reach our goal depth to detect the theorized planet. I hope to greatly improve the contrast performance with these observations, which should suffer less from saturation since the coronagraph will be used. Rather than using `PynPoint` for synthetic planet injection to calculate contrast performance, I plan to use `AppleFy` (Bonse et al., 2023) to create robust contrast curves. The `AppleFy` software holds the advantage of not assuming Gaussian noise, where out-of-the-box `PynPoint` does make this assumption. As was the case with HL Tau, the noise is unlikely to be Gaussian. This software should decrease the time required to calculate contrast, since the process is functional out-of-the-box and automated. The sensitivity I measured for HL Tau involved many hands-on steps and constant monitoring of the contrast curves. I had wanted to use `AppleFy` for the HL Tau project but decided against it due to time constraints of learning the software and the

fact that the code was not built for non-ADI reductions. In my PhD, I should be able to complete the data reduction of HD 97048 quickly enough to be able to dedicate the time necessary to use `AppleFy`, and hopefully retrieve more robust detection limits as a result. Consider the use of a coronagraph, observation of a reference star, and older age of the disk, HD 97048 should be a relatively simpler target to work with than HL Tau. I am confident that full end-to-end reduction and analysis shouldn't take more than 8 months.

Aside from JWST, I have Subaru/SCExAO data. Using the instruments CHARIS, VAMPIRES and Fast-PDI, 6 intermediate mass (IM) stars – HD 144432, HIP 80425, HIP 81474, HD 141469, HD 148352, and PDS 76 – were observed with each instrument in the hopes of making a first-time disk detection. All six IM stars have never been imaged to search for disks, but are known to have extended SED's which could indicate a disk presence. The goal is to use SCExAO's new Fast-PDI mode to obtain a bias-free sample of spiral arms statistics in disks. This work will be different to what I have done with HL Tau, in not only observing mode, but style of workflow. While HL Tau was a well-understood target with hundreds of previous observations, where the only new variable was the instrument used to observe it, all six of these targets will push the envelope further by observing new targets with a relatively new instrument. The observations of HL Tau, and even HD 97048, can be compared to previous ones and there is an expectation of what will be seen. In this SCExAO program, I have no expectations for how these data will look, and whether or not I make disk detections will directly impact how I approach the project. There is a certain level of innovation and adaptability that comes with completely new observations that I look forward to working through with these data. JWST/NIRCam's HL Tau was an introduction to this field, I am ready for the next stage.

Bibliography

ALMA Partnership, Brogan, C. L., Pérez, L. M., et al. 2015, ApJ, 808, L3, doi: 10.1088/2041-8205/808/1/L3

Amara, A., & Quanz, S. P. 2012, MNRAS, 427, 948, doi: 10.1111/j.1365-2966.2012.21918.x

Aoyama, Y., Ikoma, M., & Tanigawa, T. 2018, ApJ, 866, 84, doi: 10.3847/1538-4357/aadc11

Armitage, P. J. 2020, Astrophysics of planet formation, Second Edition

Bae, J., Hartmann, L., & Zhu, Z. 2015, ApJ, 805, 15, doi: 10.1088/0004-637X/805/1/15

Baraffe, I., Chabrier, G., Allard, F., & Hauschildt, P. 2003, in Brown Dwarfs, ed. E. Martín, Vol. 211, 41

Benisty, M., Juhasz, A., Boccaletti, A., et al. 2015, A&A, 578, L6, doi: 10.1051/0004-6361/201526011

Bitsch, B., Lambrechts, M., & Johansen, A. 2015, A&A, 582, A112, doi: 10.1051/0004-6361/201526463

Boley, A. C. 2017, ApJ, 850, 103, doi: 10.3847/1538-4357/aa93d7

Bollati, F., Lodato, G., Price, D. J., & Pinte, C. 2021, Monthly Notices of the Royal Astronomical Society, 504, 5444–5454, doi: 10.1093/mnras/stab1145

Bonse, M. J., Garvin, E. O., Gebhard, T. D., et al. 2023, AJ, 166, 71, doi: 10.3847/1538-3881/acc93c

Boss, A. P. 1997, Science, 276, 1836, doi: 10.1126/science.276.5320.1836

Brandl, B., Bettonvil, F., van Boekel, R., et al. 2021, The Messenger, 182, 22, doi: 10.18727/0722-6691/5218

Brandl, B. R., Lenzen, R., Pantin, E., et al. 2012, in Society of Photo-Optical Instrumentation Engineers (SPIE) Conference Series, Vol. 8446, Ground-based and Airborne Instrumentation for Astronomy IV, ed. I. S. McLean, S. K. Ramsay, & H. Takami, 84461M, doi: 10.1117/12.926057

Carter, A. L., Hinkley, S., Kammerer, J., et al. 2023, ApJ, 951, L20, doi: 10.3847/2041-8213/acd93e

Chabrier, G., Baraffe, I., Allard, F., & Hauschildt, P. 2000, ApJ, 542, 464, doi: 10.1086/309513

Close, L. M., Roddier, F., J. Northcott, M., Roddier, C., & Elon Graves, J. 1997, ApJ, 478, 766, doi: 10.1086/303813

Cohen, M. 1983, ApJ, 270, L69, doi: 10.1086/184072

Cugno, G., Pearce, T. D., Launhardt, R., et al. 2023, A&A, 669, A145, doi: 10.1051/0004-6361/202244891

Cugno, G., Leisenring, J., Wagner, K. R., et al. 2024, arXiv e-prints, arXiv:2401.02834, doi: 10.48550/arXiv.2401.02834

Currie, T., Lawson, K., Schneider, G., et al. 2022, Nature Astronomy, 6, 751, doi: 10.1038/s41550-022-01634-x

de Boer, J., Langlois, M., van Holstein, R. G., et al. 2020, A&A, 633, A63, doi: 10.1051/0004-6361/201834989

Dipierro, G., Price, D., Laibe, G., et al. 2015, MNRAS, 453, L73, doi: 10.1093/mnrasl/slv105

Dong, R., Li, S., Chiang, E., & Li, H. 2017, ApJ, 843, 127, doi: 10.3847/1538-4357/aa72f2

—. 2018, ApJ, 866, 110, doi: 10.3847/1538-4357/aadadd

Dong, R., Zhu, Z., & Whitney, B. 2015, ApJ, 809, 93, doi: 10.1088/0004-637X/809/1/93

Emsenhuber, A., Mordasini, C., Burn, R., et al. 2021, A&A, 656, A69, doi: 10.1051/0004-6361/202038553

Garufi, A., Podio, L., Codella, C., et al. 2021, A&A, 645, A145, doi: 10.1051/0004-6361/202039483

—. 2022, A&A, 658, A104, doi: 10.1051/0004-6361/202141264

Ginski, C., Stolker, T., Pinilla, P., et al. 2016, A&A, 595, A112, doi: 10.1051/0004-6361/201629265

Girard, J. H., Leisenring, J., Kammerer, J., et al. 2022, JWST/NIRCam Coronagraphy: Commissioning and First On-Sky Results. https://arxiv.org/abs/2208.00998

Goldreich, P., & Ward, W. R. 1973, ApJ, 183, 1051, doi: 10.1086/152291

Gonzalez, J. F., Laibe, G., & Maddison, S. T. 2017, MNRAS, 467, 1984, doi: 10.1093/mnras/stx016

Grasdalen, G. L., Strom, S. E., Strom, K. M., et al. 1984, ApJ, 283, L57, doi: 10.1086/184333

Green, J. J., Beichman, C., Basinger, S. A., et al. 2005, in Society of Photo-Optical Instrumentation Engineers (SPIE) Conference Series, Vol. 5905, Techniques and Instrumentation for Detection of Exoplanets II, ed. D. R. Coulter, 185–195, doi: 10.1117/12.619343

Gupta, A., Miotello, A., Williams, J. P., et al. 2024, arXiv e-prints, arXiv:2401.10403, doi: 10.48550/arXiv.2401.10403

Hammond, I., Christiaens, V., Price, D. J., et al. 2023, MNRAS, 522, L51, doi: 10.1093/mnrasl/slad027

Heap, S. R., Lindler, D. J., Lanz, T. M., et al. 2000, The Astrophysical Journal, 539, 435

Helled, R., Bodenheimer, P., Podolak, M., et al. 2014, in Protostars and Planets VI, ed. H. Beuther, R. S. Klessen, C. P. Dullemond, & T. Henning, 643–665, doi: 10.2458/azu_uapress_9780816531240-ch028

Jin, S., Li, S., Isella, A., Li, H., & Ji, J. 2016, ApJ, 818, 76, doi: 10.3847/0004-637X/818/1/76

Johansen, A., & Lambrechts, M. 2017, Annual Review of Earth and Planetary Sciences, 45, 359, doi: 10.1146/annurev-earth-063016-020226

Kanagawa, K. D., Muto, T., Tanaka, H., et al. 2015, ApJ, 806, L15, doi: 10.1088/2041-8205/806/1/L15

Keppler, M., Benisty, M., Müller, A., et al. 2018, A&A, 617, A44, doi: 10.1051/0004-6361/201832957

Kuhn, J. R., Potter, D., & Parise, B. 2001, ApJ, 553, L189, doi: 10.1086/320686

Lafrenière, D., Marois, C., Doyon, R., & Barman, T. 2009, ApJ, 694, L148, doi: 10.1088/0004-637X/694/2/L148

Lambrechts, M., & Johansen, A. 2012, A&A, 544, A32, doi: 10.1051/0004-6361/201219127

Leisenring, J. M., Skrutskie, M. F., Hinz, P. M., et al. 2012, in Society of Photo-Optical Instrumentation Engineers (SPIE) Conference Series, Vol. 8446, Ground-based and Airborne Instrumentation for Astronomy IV, ed. I. S. McLean, S. K. Ramsay, & H. Takami, 84464F, doi: 10.1117/12.924814

Linder, E. F., Mordasini, C., Mollière, P., et al. 2019, A&A, 623, A85, doi: 10.1051/0004-6361/201833873

Lodato, G., Dipierro, G., Ragusa, E., et al. 2019, MNRAS, 486, 453, doi: 10.1093/mnras/stz913

Long, F., Pinilla, P., Herczeg, G. J., et al. 2018, ApJ, 869, 17, doi: 10.3847/1538-4357/aae8e1

Marley, M. S., Fortney, J. J., Hubickyj, O., Bodenheimer, P., & Lissauer, J. J. 2007, ApJ, 655, 541, doi: 10.1086/509759

Marois, C., Lafrenière, D., Doyon, R., Macintosh, B., & Nadeau, D. 2006, ApJ, 641, 556, doi: 10.1086/500401

Matsuo, T., Shibai, H., Ootsubo, T., & Tamura, M. 2007, in In the Spirit of Bernard Lyot: The Direct Detection of Planets and Circumstellar Disks in the 21st Century, ed. P. Kalas, 18

Mordasini, C., Alibert, Y., Klahr, H., & Henning, T. 2012, A&A, 547, A111, doi: 10.1051/0004-6361/201118457

Mullin, C., Dong, R., Leisenring, J., et al. 2024, AJ, 167, 183, doi: 10.3847/1538-3881/ad2de9

Mundt, R., & Fried, J. W. 1983, ApJ, 274, L83, doi: 10.1086/184155

Murakawa, K., Oya, S., Pyo, T. S., & Ishii, M. 2008, A&A, 492, 731, doi: 10.1051/0004-6361:200810723

Müller, A., Keppler, M., Henning, T., et al. 2018, Astronomy &amp Astrophysics, 617, L2, doi: 10.1051/0004-6361/201833584

Ormel, C. W., & Klahr, H. H. 2010, A&A, 520, A43, doi: 10.1051/0004-6361/201014903

Ormel, C. W., Vazan, A., & Brouwers, M. G. 2021, A&A, 647, A175, doi: 10.1051/0004-6361/202039706

Paardekooper, S.-J., Dong, R., Duffell, P., et al. 2022, arXiv e-prints, arXiv:2203.09595, doi: 10.48550/arXiv.2203.09595

Pearson, S. G., & McCaughrean, M. J. 2023, arXiv e-prints, arXiv:2310.01231, doi: 10.48550/arXiv.2310.01231

Perrin, M. D., Sivaramakrishnan, A., Lajoie, C.-P., et al. 2014, in Society of Photo-Optical Instrumentation Engineers (SPIE) Conference Series, Vol. 9143, Space Telescopes and Instrumentation 2014: Optical, Infrared, and Millimeter Wave, ed. J. Oschmann, Jacobus M., M. Clampin, G. G. Fazio, & H. A. MacEwen, 91433X, doi: 10.1117/12.2056689

Pinilla, P., Birnstiel, T., Ricci, L., et al. 2012, A&A, 538, A114, doi: 10.1051/0004-6361/201118204

Pinilla, P., de Juan Ovelar, M., Ataiee, S., et al. 2015, A&A, 573, A9, doi: 10.1051/0004-6361/201424679

Pinte, C., van der Plas, G., Ménard, F., et al. 2019, Nature Astronomy, 3, 1109, doi: 10.1038/s41550-019-0852-6

Pollack, J. B., Hubickyj, O., Bodenheimer, P., et al. 1996, icarus, 124, 62, doi: 10.1006/icar.1996.0190

Rafikov, R. R. 2004, in Astronomical Society of the Pacific Conference Series, Vol. 316, Order and Chaos in Stellar and Planetary Systems, ed. G. G. Byrd, K. V. Kholshevnikov, A. A. Myllri, I. I. Nikiforov, & V. V. Orlov, 132, doi: 10.48550/arXiv.astro-ph/0310392

Rebull, L. M., Wolff, S. C., & Strom, S. E. 2004, AJ, 127, 1029, doi: 10.1086/380931

Reggiani, M., Quanz, S. P., Meyer, M. R., et al. 2014, ApJ, 792, L23, doi: 10.1088/2041-8205/792/1/L23

Rice, W. K. M., Armitage, P. J., Wood, K., & Lodato, G. 2006, MNRAS, 373, 1619, doi: 10.1111/j.1365-2966.2006.11113.x

Rieke, M. J., Kelly, D. M., Misselt, K., et al. 2023, PASP, 135, 028001, doi: 10.1088/1538-3873/acac53

Safranov, V. S., & Ziglina, I. N. 1991, Solar System Research, 25, 139

Schneider, G., Thompson, R. I., Smith, B. A., & Terrile, R. J. 1998, in Society of Photo-Optical Instrumentation Engineers (SPIE) Conference Series, Vol. 3356, Space Telescopes and Instruments V, ed. P. Y. Bely & J. B. Breckinridge, 222–233, doi: 10.1117/12.324461

Sengupta, S., & Marley, M. S. 2010, ApJ, 722, L142, doi: 10.1088/2041-8205/722/2/L142

Skidmore, W., TMT International Science Development Teams, & Science Advisory Committee, T. 2015, Research in Astronomy and Astrophysics, 15, 1945, doi: 10.1088/1674-4527/15/12/001

Soummer, R., Pueyo, L., & Larkin, J. 2012, ApJ, 755, L28, doi: 10.1088/2041-8205/755/2/L28

Speedie, J., & Dong, R. 2022, in Disks and Planets across ESO Facilities, 12, doi: 10.5281/zenodo.7444182

Spiegel, D. S., & Burrows, A. 2012, ApJ, 745, 174, doi: 10.1088/0004-637X/745/2/174

Stapelfeldt, K. R., Burrows, C. J., Krist, J. E., et al. 1995, ApJ, 449, 888, doi: 10.1086/176106

Stephens, I. W., Yang, H., Li, Z.-Y., et al. 2017, ApJ, 851, 55, doi: 10.3847/1538-4357/aa998b

Stolker, T., Bonse, M. J., Quanz, S. P., et al. 2019, A&A, 621, A59, doi: 10.1051/0004-6361/201834136

Stolker, T., Min, M., Stam, D. M., et al. 2017, A&A, 607, A42, doi: 10.1051/0004-6361/201730780

Takahashi, S. Z., & Inutsuka, S.-i. 2014, ApJ, 794, 55, doi: 10.1088/0004-637X/794/1/55

Testi, L., Skemer, A., Henning, T., et al. 2015, ApJ, 812, L38, doi: 10.1088/2041-8205/812/2/L38

van der Marel, N., Dong, R., di Francesco, J., Williams, J. P., & Tobin, J. 2019, ApJ, 872, 112, doi: 10.3847/1538-4357/aafd31

Wagner, K., Leisenring, J., Cugno, G., et al. 2024, arXiv e-prints, arXiv:2401.02830, doi: 10.48550/arXiv.2401.02830

Weidenschilling, S. J. 1977, MNRAS, 180, 57, doi: 10.1093/mnras/180.2.57

White, R. J., & Hillenbrand, L. A. 2004, ApJ, 616, 998, doi: 10.1086/425115

Williams, J. P., & Cieza, L. A. 2011, ARA&A, 49, 67, doi: 10.1146/annurev-astro-081710-102548

Yen, H.-W., Gu, P.-G., Hirano, N., et al. 2019, ApJ, 880, 69, doi: 10.3847/1538-4357/ab29f8

Youdin, A. N., & Goodman, J. 2005, ApJ, 620, 459, doi: 10.1086/426895

Zhu, Z., Nelson, R. P., Dong, R., Espaillat, C., & Hartmann, L. 2012, ApJ, 755, 6, doi: 10.1088/0004-637X/755/1/6

Appendix A

Additional Figures

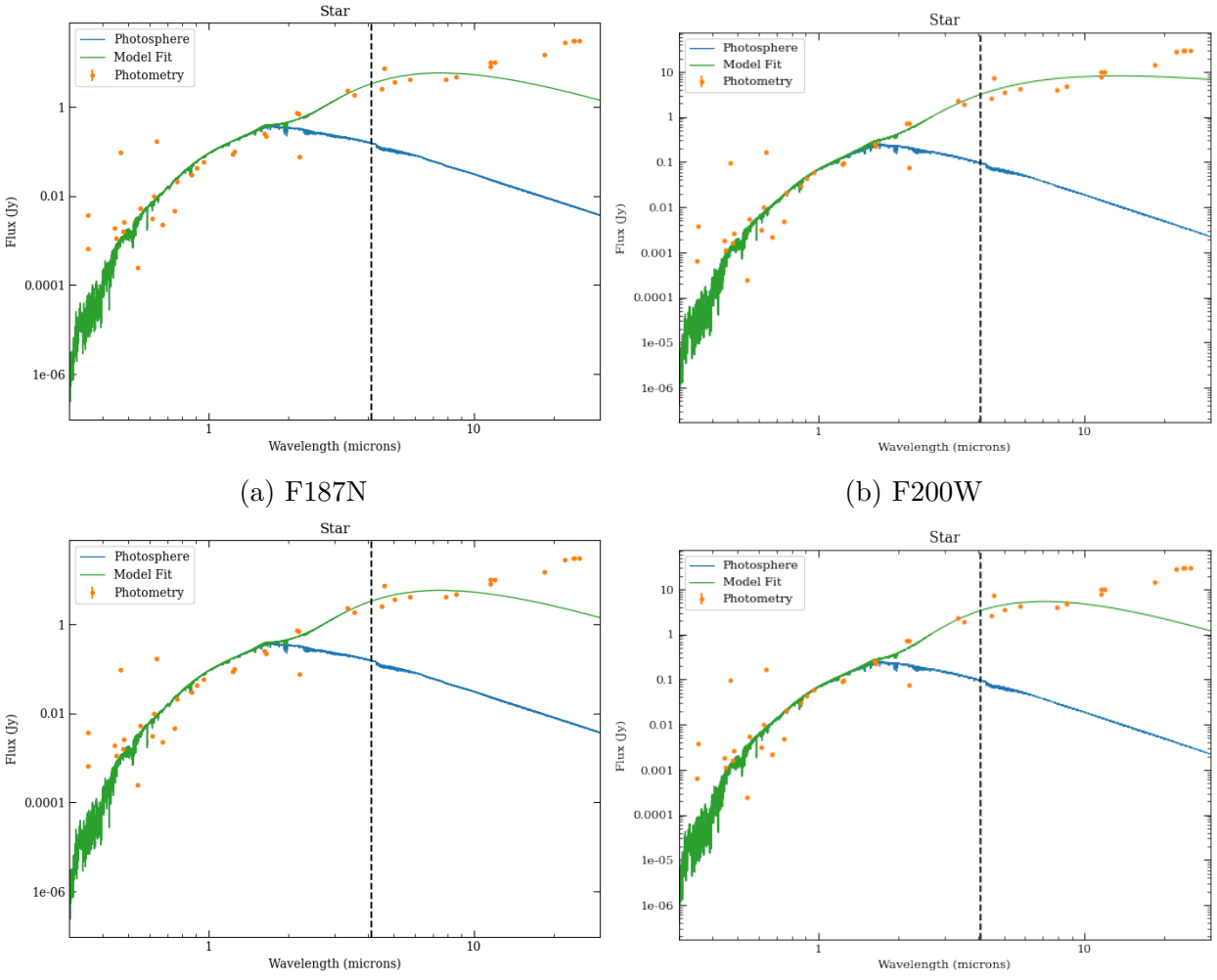

(a) F187N

(b) F200W

(c) F405N

(d) F410M

Figure A.1: SEDs to create `webbpsf`s for each filter.

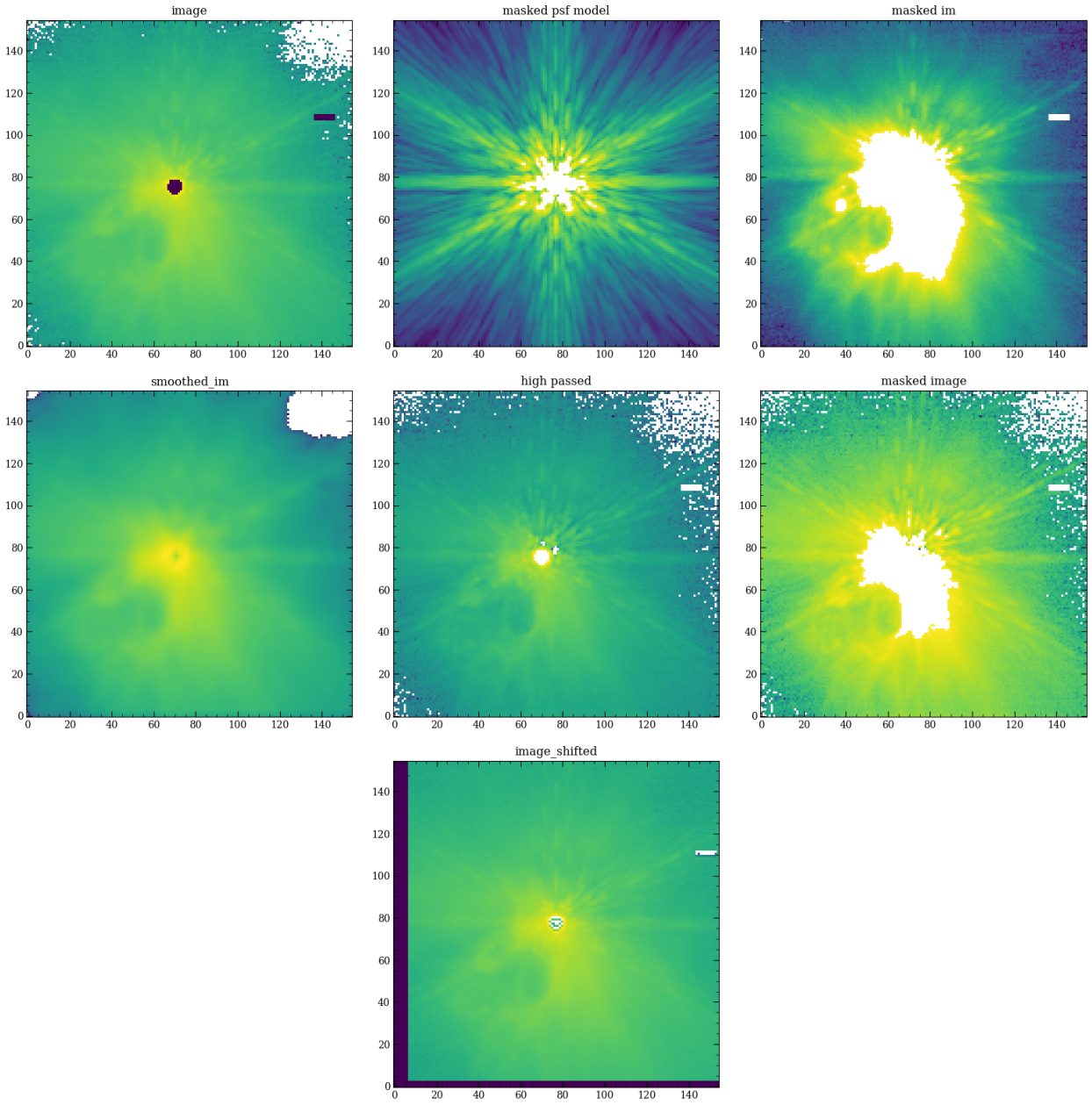

Figure A.2: Centering process demonstrated on one F200W roll angle. The workflow follows left to right.

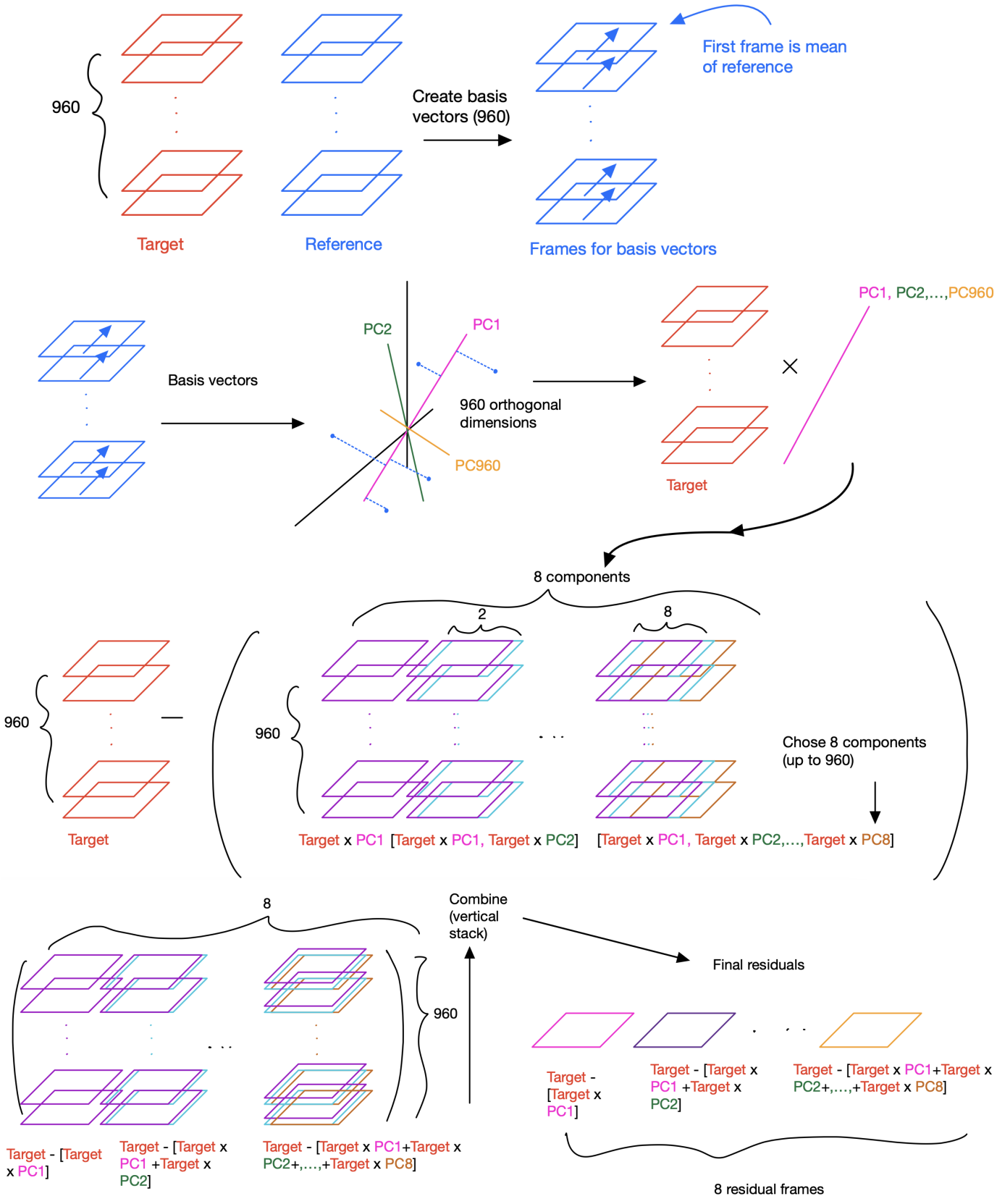

Figure A.3: Visual for the workflow of PCA PSF subtraction. Diagrams drawn by me.

Appendix B

Calculations

B.1 Flux derivation

By definition of magnitude,

$$m1 - m2 = -2.5log(\frac{f1}{f2})$$

Taking apparent magnitude m and absolute magnitude M,

$$m - M = 5log(d) + 5 = 2.5log((\frac{d}{10})^2)$$
$$M - m = -2.5log((\frac{d}{10})^2)$$

Since $M - m$ is just a ratio of magnitudes, we can write,

$$M - m = -2.5log(\frac{f_{10}}{f_p})$$
$$log(\frac{f_{10}}{f_p}) = log((\frac{d}{10})^2)$$
$$log(f_{10}) = log(f_p \times (\frac{d}{10})^2)$$

where $log(f_{10})$ is the logged flux that should appear in the isochrone table.